Water Resources Research

RESEARCH ARTICLE
10.1029/2023WR035989

Stochastic Modeling of Thin Mud Drapes Inside Point Bar Reservoirs With ALLUVSIM-GANSim

Xun Hu[1,2,3], **Suihong Song**[4], **Jiagen Hou**[1,2], **Yanshu Yin**[5], **Mingqiu Hou**[6], and **Leonardo Azevedo**[3]

[1]State Key Laboratory of Petroleum Resources and Prospecting, China University of Petroleum (Beijing), Beijing, China, [2]College of Geosciences, China University of Petroleum (Beijing), Beijing, China, [3]DER/CERENA, Instituto Superior Técnico, Universidade de Lisboa, Lisbon, Portugal, [4]Department of Energy Science and Engineering, Stanford University, Stanford, CA, USA, [5]Yangtze University, Wuhan, China, [6]Research Institute of Petroleum Exploration and Development (PetroChina), Beijing, China

Key Points:

- The proposed method achieves fast conditional mud drapes stochastic modeling
- The effectiveness and applicability of the proposed method have been verified in modern channel deposit
- The proposed method provides technical support for future predictions of mud drapes inside underground point bar reservoirs

Supporting Information:

Supporting Information may be found in the online version of this article.

Correspondence to:

S. Song and Y. Yin,
suihong@stanford.edu;
yys6587@126.com

Citation:

Hu, X., Song, S., Hou, J., Yin, Y., Hou, M., & Azevedo, L. (2024). Stochastic modeling of thin mud drapes inside point bar reservoirs with ALLUVSIM-GANSim. *Water Resources Research*, *60*, e2023WR035989. https://doi.org/10.1029/2023WR035989

Received 1 AUG 2023
Accepted 24 MAY 2024

Author Contributions:

Funding acquisition: Jiagen Hou, Leonardo Azevedo
Methodology: Xun Hu, Suihong Song
Project administration: Jiagen Hou
Supervision: Xun Hu, Suihong Song, Jiagen Hou, Yanshu Yin, Leonardo Azevedo
Writing – original draft: Xun Hu
Writing – review & editing: Xun Hu, Suihong Song, Yanshu Yin, Mingqiu Hou, Leonardo Azevedo

Abstract Modeling inclined fine-scale mud drapes inside point bars, deposited on accretion surfaces during stages of low energy or slack water, is critical to modeling fluid flow in complex sedimentary environments (e.g., fluvial and turbidity flows). These features have been modeled using deterministic or geostatistical modeling tools (e.g., object-, event-, and pixel-based). However, this is a non-trivial task due to the need to preserve geological realism (e.g., connectivity within sedimentary features and facies hierarchy), while being able to condition the generated models to point data (e.g., well data). Generative Adversarial Networks (GAN) have been successfully applied to reproduce several large-scale scenarios (e.g., braided rivers and carbonate reservoirs), yet their potential for capturing small-scale and hierarchical features remains largely unexplored. Here, we propose a geo-modeling workflow for fast modeling of small-scale conditional mud drapes based on ALLUVSIM and GANSim. Initially, improved ALLUVSIM produces realistic unconditional models of mud drapes along accretionary surfaces, serving as GAN training data. GANSim is then employed to achieve conditioning to well data and probability maps derived from geophysical modeling. Finally, temporal pressure data observed in wells are further conditioned via a Markov chain Monte Carlo sampling method. The proposed geo-modeling workflow is validated in a two-dimensional synthetic example as the pre-trained generator extracts mud-drapes-features and generates multiple facies realizations conditioned to diverse information. A field application example in a modern meandering river verifies the effectiveness and practicability of the proposed workflow in real case application examples. The application examples illustrate the potential of the proposed method to predict mud drapes inside point bar reservoirs.

1. Introduction

Geology is composed of a hierarchy of heterogeneities. Even within a pure sandy point bar of a meandering channel (e.g., fluvial, mixed tidal-fluvial, tidal, or marine channel), there might exist many inclined, thin, muddy beds that hinder the subsurface fluid flow, such as CO_2, water, and oil (Biber et al., 2017; Dawuda & Srinivasan, 2022b; Johnson & Dashtgard, 2014; Makaske & Weerts, 2005; Novakovic et al., 2002; Willis & White, 2000). Such muddy low permeability beds (i.e., flow baffles) with depositional dip are commonly designated as "mud (shale) drapes" (Colombera et al., 2018; Li & White, 2003; Pranter et al., 2007; Thomas et al., 1987; Yan et al., 2017; Yin, 2013). Mud drapes often have a nearly parallel strike with the active or abandoned channels with a sheet-like geometry, ranging from millimeters to centimeters in thickness. They are composed of fine lithologies, such as mudstone, siltstone, or claystone. Mud drapes are probably deposited during a single major flood event as flood energy wanes, with fine-grained lithologies draping and depositing on the point bar sand (Bridge & Diemer, 1983; Thomas et al., 1987). Being able to realistically model these mud drapes distributions, that are consistent with given sparse well facies interpretations, geophysical data, temporal pressure change data observed at wells, and some global features like the proportion of each facies, are of significance in the geological storage of CO_2, subsurface water management and hydrocarbon production.

Modeling the spatial distribution of mud drapes is commonly achieved through hierarchical modeling of channel belts, single channels, point bar sand bodies, and finally mud drapes inside point bars. There has been an effort to predict the spatial distribution of large-scale channel belts deposits (Dupont et al., 2018; Nesvold & Mukerji, 2021; Rongier et al., 2017; Sun et al., 2023; Winkels et al., 2022). However, accurately modeling the mud drapes is challenging because the mud drape is often thin, below the seismic resolution limits (Li &

White, 2003), and therefore their presence and geometry are hard to model. Additionally, their spatial geological patterns are complex, and conditioning to various sources of data, such as well-interpreted facies data and global features like the distance between successive drapes and thickness, is challenging.

Object-based methods (OBM) are extensively used in the field of fluvial reservoir modeling (e.g., FLUVSIM algorithm) (Deutsch & Tran, 2002). In this class of methodologies, the geometries of fluvial architectural elements (i.e., fluvial sedimentary objects) are described by user-defined parameters and mud drapes are simulated along parallel curves in the plan (e.g., Hassanpour et al., 2013; Yin, 2013) and sigmoidal functions in vertical profiles (e.g., Dawuda & Srinivasan, 2022a). With these algorithms, the simulated mud drapes may lack geological realism.

Compared to OBM, process-based/process-mimicking-based (Pyrcz & Deutsch, 2004; Shu et al., 2015) and geometric-based methods (Montero et al., 2021; Yan et al., 2017, 2021) may be more suitable for characterizing the distribution and geometries of point bars and their internal mud drapes geometries. For example, the bank retreat fluvial model is a simplified process-based model of stream meander migration, where the stream and its migration process are parameterized by hydraulic parameters (Howard, 1992; Howard & Knutson, 1984), applied to construct realistic models of channel belt fluvial reservoirs (Lopez et al., 2001; Sun et al., 1996). The ALLUVSIM algorithm (Pyrcz et al., 2009) further adopts the bank retreat fluvial model to characterize the meander migration and to create various reliable fluvial styles, but mud drapes are not considered. Pyrcz and Deutsch (2004) used an unconditional bank retreat fluvial model to reproduce the complex geometries of mud drapes. Shu et al. (2015) proposed a meander migration process to simulate conditional mud drapes using an inversion algorithm. Although the forward and/or backward simulation based on river hydrodynamics can accurately characterize the geometry of point bars and mud drapes, conditioning to borehole data or seismic data is a long-standing challenge.

Two-point statistics (TPS)-based (Deutsch & Journel, 1998) and multiple-point statistics (MPS)-based methods (Mariéthoz & Caers, 2014) are commonly used for generating subsurface models that address the data conditioning problem. Li and White (2003) utilized ground-penetrating radar-derived variograms to model stochastic mud drapes in distributary channel point bars. Montero et al. (2021) and Wang et al. (2021) employed MPS to simulate mud drapes in three-dimensions for theoretical and real fluvial reservoirs, respectively. While MPS-based methods offer greater realism compare to TPS-based methods, their application in modeling nonstationary spatial phenomena, particularly in mud drapes, remains challenging. Rongier et al. (2017) proposed using TPS (sequential Gaussian simulation) or MPS methods to simulate migration factor to constrain forward and backward channel migration processes, yet the incorporation of mud drapes and data conditioning requires further exploration.

Generative Adversarial Networks (GAN) have two different deep neural networks that are trained adversarial (i.e., a generator and a discriminator) (Goodfellow et al., 2014). GAN can be implemented using various types of neural network architectures, such as fully connected networks; Convolutional neural networks (CNN) (e.g., Lecun et al., 1998); Long-short-term memory (LSTM) (e.g., Hochreiter & Schmidhuber, 1997). During training, GAN alternates between the training of the discriminator and the generator, using loss functions such as Wasserstein loss (Arjovsky et al., 2017) and its penalty versions (Gulrajani et al., 2017). GAN excels at capturing and reproducing complex spatial patterns, making them highly useful in many computer vision applications such as image translation (e.g., Park et al., 2019) and video segmentation (e.g., Kirillov et al., 2023). GAN has been widely used within the geo-modeling workflow (e.g., Azevedo et al., 2020; Laloy et al., 2018; Song et al., 2021a, 2021b; Song, Mukerji, & Hou et al., 2022). Laloy et al. (2018) and Zhang et al. (2019) applied GAN for the geomodeling of 2-D/3-D channel facies geomodels and achieved conditioning to borehole data and temporal pressure data. However, their approaches are computationally expensive. Whenever the observed data change, finding an appropriate latent vector becomes necessary, involving techniques like Markov chain Monte Carlo (McMC) (e.g., Laloy et al., 2018), gradient decent (e.g., Zhang et al., 2019) and inference network training (e.g., Chan & Elsheikh, 2019). Thus, Song et al. (2021a) and Song, Mukerji, Hou, Zhang, et al. (2022) proposed an advanced GAN-based geomodeling method with direct conditioning, called GANSim, where the generator takes conditioning data (i.e., sparse well-interpreted facies data, geophysics-produced probability maps, and global features like channel width and sinuosity) as inputs; after training, the trained generator can produce realistic geomodels that are consistent with the given conditioning data. Song, Mukerji, Hou and Zhang, et al. (2022) extended the use of GANSim to model real karst caves reservoirs, achieving excellent performance in generating

realistic facies patterns. Also, GANSim has been combined with different latent vector searching algorithms to further achieve conditioning to temporal borehole pressure data (Song et al., 2023).

Most of the existing application examples where GAN has been successfully applied focus on validating methods, which results in unrealistic or simplified training data (e.g., simple training image with two facies and with relatively simple geometries) (Strebelle, 2002). In this work, we aim to combine ALLUVSIM's high-quality realism and GANSim's pattern reproduction and conditional ability to simulate small-scale mud drapes under various types of conditioning data. Our goal in the stochastic geomodeling of mud drapes is to devise an effective workflow for producing geological patterns of mud drapes including their geometries, their distance between each other, and the contact relationships with other facies, and easily achieving ideal static data conditioning and history matching in modern river surface.

This paper is organized as follows. After detailing the adopted methodology in the next section, we describe how to build geologically plausible mud drapes geomodels as the training data set shown in Section 3. Then, based on the training data set, we apply GAN for unconditional geomodeling of mud drapes in Section 4. Next, in Section 5, we further apply GANSim to train a CNN-based conditional generator to produce facies models conditioned to well interpretations and geophysics-produced facies probability maps. The generator's performance is assessed using different quantitative metrics. In Section 6, a history-matching experiment in modern channel deposits is designed to verify the effectiveness and applicability of the pre-trained generator using ALLUVSIM-GANSim. Meanwhile, McMC is used to condition the GANSim-produced facies models further to temporal pressure change data observed at wells. Finally, conclusions are given in Section 7.

2. Methodology

This section details the ALLUVSIM algorithm, which is used to generate the training data set, the proposed GAN to generate mud drapes facies, which is based on conditional progressive growing of GAN (PgGAN) (Karras et al., 2017) under the GANSim workflow, and the proposed GANsim-based history matching method.

2.1. ALLUVSIM for Simulating Mud Drapes Models

The ALLUVSIM algorithm is well-suited for constructing fluvial models (Pyrcz et al., 2009) and extended successfully to diverse depositional environments like confined deep water settings (Yin, Hu, et al., 2020). Using a fluvial sedimentary object's central axis, termed a centerline, it establishes initial channel centerlines of various sinuosity levels via Ferguson's disturbed periodic model (1976). Channel migration centerlines are then determined based on the bank retreat model (Howard, 1992; Sun et al., 1996) and organized into groups called a centerline complex (Figure 1a). This forms the basis for simulating fluvial objects like channel fills and point bars but overlooks mud drapes in temporal sequence (Figure 1b).

To address this limitation, we incorporate the extension length ratio and frequency of mud drapes (i.e., improved ALLUVSIM). Initially, channel boundaries are randomly retained as mud drapes during the meandering process (Li & Caers, 2011; Pyrcz & Deutsch, 2004), accounting for their varying frequency, as fine lithologies often drape there when flood energy diminishes (Thomas et al., 1987). Then, mud drapes on the concave (outer) bank are replaced with channel sand due to erosion. Lastly, considering their diverse extension distances, we randomly preserve these mud drapes on the convex (inner) bank, as the increasing flow energy often truncate their lower parts. This approach results in the formation of "semi-connected sand-body" models, referred to as mud drapes models (Figure 1c).

Moreover, sinuosity is introduced to control the generation of low- and high-sinuosity channels, indirectly calculated by dividing the current channel length by the initial channel length and then multiplying it by the initial channel sinuosity (Yin, Hu, et al., 2020). Lateral channel migration continues until the current channel's sinuosity reaches the target value. Consequently, the outcome is a set of semi-connected mud drapes models, each possessing a desired sinuosity (Figure 1c).

2.2. Progressive Growing of GAN (PgGAN) for Unconditional Geomodeling

In classical GAN (Supporting Information S1), the generator and discriminator networks are typically trained at a fixed-resolution image and simultaneously learn features of different scales from images. This approach often

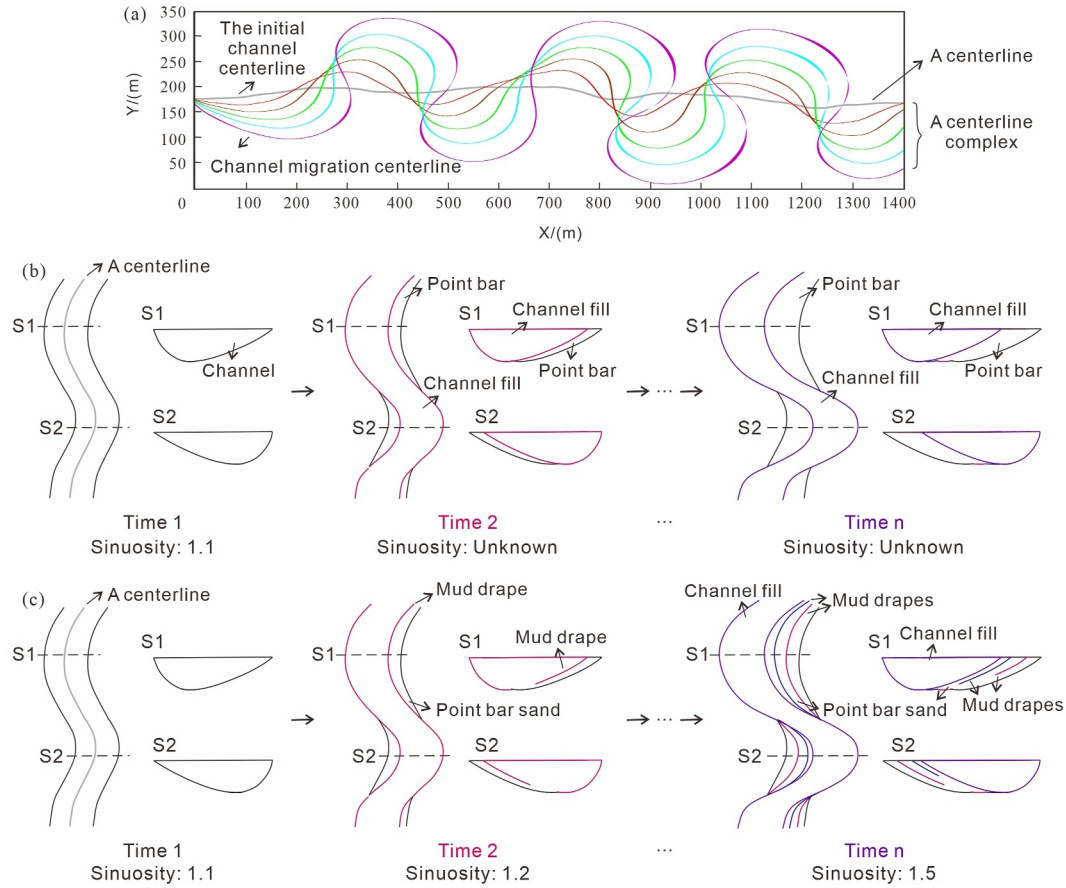

Figure 1. (a) A centerline complex displaying lateral and downstream migration of the initial channel centerline (gray line). (b) An illustration of point bar formation over time in original ALLUVSIM. The last channel is the channel fill facies type and the previous channel is the point bar facies type. (c) An illustration of the mud drapes over time in improved ALLUVSIM. Each step includes preserving and removing channel bottom surfaces, resulting in lateral continuity or discontinuity of mud drapes preservation based on extension length and development frequency.

causes the generated images to be blurry and lacking the fine details of the training data set. Besides, mode collapsing often occurs in classical GAN (i.e., the trained generator cannot produce variable facies models).

To overcome these challenges, Wasserstein loss with gradient penalty, mini-batch standard deviation, and progressive growing are used in PgGAN (Karras et al., 2017). With the progressive growing technique, the training of the generator progressively captures different-scale features from low-to-high and accordingly produces different-resolution images from low-to-high. For example, the generated images may start from a 4 by 4-pixel image and double the resolution until the final 64 by 64-pixel image (Figure 2). This gradual growth helps reduce reliance on nearest neighbor upsampling and increase reliance on learned parameters, controlled by the parameter α, which grows from 0 to 1 in increments.

For our specific application of unconditional geomodeling, we use the architecture of unconditional generator and discriminator networks shown in Table 1. When comparing with Song et al. (2021b), we mainly modify the generator by replacing fully-connected and reshape layers with convolutional layers, enabling the trained generator to produce images at large sizes instead of the same fixed size as the training data. For example, with the generator architecture of Table 1, if the size of the latent vector is multiplied from 4 by 4 by 8 into 8 by 12 by 8, then the generator's output would also enlarge from 64 by 64 to 128 by 192 pixels.

To assess the performance of the GAN, we employ one qualitative (visual inspection) and two quantitative metrics: namely variogram model analysis; and a dimension reduction method by combining sliced Wasserstein distance and multidimensional scaling (SWD-MDS) (Song et al., 2021b). With SWD-MDS, a random facies

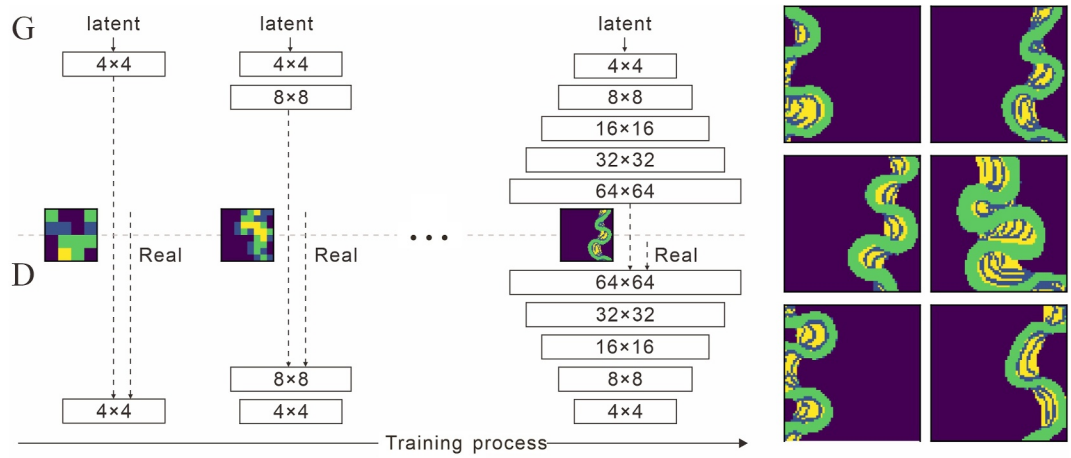

Figure 2. The training process of mud drapes images using progressive growing of GAN. Starting at a low spatial 4 × 4 pixels resolution, the generator (G) and discriminator (D) gradually increase to a higher 64 × 64 pixels resolution. Here, N×N represents convolutional layers operating on $N \times N$ resolution. Facies models include floodplain (black), mud drapes (blue), channel fill (green), and point bar (yellow) types. The right shows six mud drapes images generated using progressive growing at 64 × 64 (modified by Karras et al. (2017)).

model can be projected into a point of a low-dimensional space (e.g., 2-D or 3-D); when multiple facies models are projected, the distribution of these low-dimensional points represents the geological patterns of these facies models. These metrics evaluate the quality and geological plausibility of the generated images compared to the original training data set.

2.3. Conditional GAN

Figure 3 shows a schematic representation of conditional PgGAN under a conditional GANSim workflow. This variant differs from the unconditional GAN (Section 2.2) primarily in two aspects: the generator architecture and the condition-based loss functions.

Regarding the generator architecture, the conditional GAN incorporates the input conditioning data, specifically well-interpreted facies data denoted as "w" and probability data "p", which are progressively combined with the input latent vector "z." For example, during the 16 by 16 training phase, the original 64 by 64-resolution of the input well facies data is downsampled to 16 by 16-resolution and represented as two channels: a well location indicator channel (16 × 16 × 1) and a well facies indicator channel (16 × 16 × 1). These two channels (16 × 16 × 2) undergo convolution to form 16 channels (16 × 16 × 16), which are then added to the corresponding resolution of the generator network structure (indicated by the red solid arrows in Figure 3).

Regarding the condition-based loss functions, they play a vital role in guiding the generator to learn the relationship between the input well-interpreted facies data (or probability) and generated facies models at each resolution (Figure 3). The combined loss function used in conditional generation is expressed as follows:

$$L(D_\varphi, G_\theta)_{\text{comb}} = \beta_{\text{orig}} L(D_\varphi, G_\theta)_{\text{orig}} + \beta_{\text{well}} L(G_\theta)_{\text{well}} + \beta_{\text{prob}} L(G_\theta)_{\text{prob}} \quad (1)$$

where β_{orig}, β_{well}, and β_{prob} are the weights of the facies-pattern-based loss function $L(D_\varphi, G_\theta)_{\text{orig}}$, well-based loss function $L(G_\theta)_{\text{well}}$, and probability-based loss function $L(G_\theta)_{\text{prob}}$, respectively. By combining these loss functions, the conditional GAN can effectively integrate the information from well and probability data to generate lower uncertainty facies models.

In addition to evaluating the metrics introduced for the unconditional GAN, assessing the conditioning ability of conditional GAN on observed data is crucial. The metric involves evaluating the matching of well-

Table 1
Architectures of the Unconditional Generator and Discriminator Networks Modified From Song et al. (2021b)

Generator	Act	Output shape	Params
Latent vector	–	4 × 4 × 8	–
Conv 3 × 3	LReLU	4 × 4 × 128	9 k
Conv 3 × 3	LReLU	4 × 4 × 128	148 k
Upsample	–	8 × 8 × 128	–
Conv 3 × 3	LReLU	8 × 8 × 128	148 k
Conv 3 × 3	LReLU	8 × 8 × 128	148 k
Upsample	–	16 × 16 × 128	–
Conv 3 × 3	LReLU	16 × 16 × 128	148 k
Conv 3 × 3	LReLU	16 × 16 × 128	148 k
Upsample	–	32 × 32 × 128	–
Conv 3 × 3	LReLU	32 × 32 × 128	148 k
Conv 3 × 3	LReLU	32 × 32 × 128	148 k
Upsample	–	64 × 64 × 128	–
Conv 3 × 3	LReLU	64 × 64 × 64	74 k
Conv 3 × 3	LReLU	64 × 64 × 64	37 k
Conv 1 × 1	Linear	64 × 64 × 1	65
Total trainable parameters			1.16 M
Discriminator	**Act.**	**Output shape**	**Params**
Input image	–	64 × 64 × 1	–
Conv 1 × 1	LReLU	64 × 64 × 64	128
Conv 3 × 3	LReLU	64 × 64 × 64	37 k
Conv 3 × 3	LReLU	64 × 64 × 128	74 k
Downsample	–	32 × 32 × 128	–
Conv 3 × 3	LReLU	32 × 32 × 128	148 k
Conv 3 × 3	LReLU	32 × 32 × 128	148 k
Downsample	–	16 × 16 × 128	–
Conv 3 × 3	LReLU	16 × 16 × 128	148 k
Conv 3 × 3	LReLU	16 × 16 × 128	148 k
Downsample	–	8 × 8 × 128	–
Conv 3 × 3	LReLU	8 × 8 × 128	148 k
Conv 3 × 3	LReLU	8 × 8 × 128	148 k
Downsample	–	4 × 4 × 128	–
Minibatch stddev	–	4 × 4 × 129	–
Conv 3 × 3	LReLU	4 × 4 × 128	148 k
Fully-connected	LReLU	2,048 × 1	262 k
Fully-connected	Linear	1 × 1	2,049
Total trainable parameters			1.41 M

interpreted facies data and GAN-produced facies model, as well as the degree of matching probability map and the frequency of GAN-produced facies models.

2.4. History Matching Combining Markov Chain Monte Carlo and Conditional GAN

In the application example shown below, we predict facies m using daily measurements of bottomhole pressure (BHP) d observed at sparely spatially distributed wells. In a Bayesian framework, the posterior probability density function (pdf) is given by:

$$P(m|d) = \frac{P(d|m)\,P(m)}{P(d)} \propto L(m|d)\,P(m) \tag{2}$$

where $P(m)$ represents the prior space, $L(m|d) \equiv P(d|m)$ represents a likelihood function, and $P(d)$ is normalization constant. The likelihood function represents the degree of fit between m and d.

The objective and likelihood functions can be defined as:

$$F(m) = \frac{1}{N}\sum_{k=1}^{N}\left(f_k(m) - d_k\right)^2 \tag{3}$$

$$L(m|d) = \exp\left(-\frac{1}{N}\sum_{k=1}^{N}\frac{\left(f_k(m) - d_k\right)^2}{2\sigma^2}\right) \tag{4}$$

where N is the number of observed pressures at wells, d_k is the pressures of the k-th observation well, $f_k(m)$ is a deterministic and error-free forward process, $f_k(m) = d_k + e$, and e is the noise term with mean zero and variance σ.

The prior space is represented by multiple realizations generated by the trained generator $G_\theta(z,w,p)$. The prior pdf is formulated as:

$$P(m) = P(m|z)\,P(z) = \frac{1}{2\pi}\exp\left(-\sum_{n=1}^{128}\frac{{z_n}^2}{2}\right) \tag{5}$$

where $P(m|z)$ is the probability from low-dimensional space R^{128} to high-dimensional space $R^{64\times64}$, $P(z)$ is the pdf of a latent vector z in its distribution P_z, z_n is the n-th dimension element in the 128-dimensional latent vector, $z_n \sim \text{Gaussian}(0,1)$. Since the same random vector would map the same output in this study, we default to $P(m|z)$ equals to one.

In Metropolis-Hasting (Hastings, 1970; Metropolis et al., 1953), two steps are carried out at each iteration: (a) proposing a new model m^{i+1} using the transition matrix $q\left(m^{i+1}\middle|m^i\right)$; (b) accepting the suggested model with a certain probability $\alpha\left(m^i,m^{i+1}\right)$; otherwise, retain the previous model m^i. The acceptance rate of the suggested model can be expressed as follow:

$$\alpha\left(m^i,m^{i+1}\right) = \min\left\{1,\frac{L\left(m^{i+1}|d\right)}{L\left(m^i|d\right)}\right\} = \min\left\{1,\exp\left(\frac{1}{N}\sum_{k=1}^{N}\frac{\left(f_k\left(m^i\right)-d_k\right)^2-\left(f_k\left(m^{i+1}\right)-d_k\right)^2}{2\sigma^2}\right)\right\} \tag{6}$$

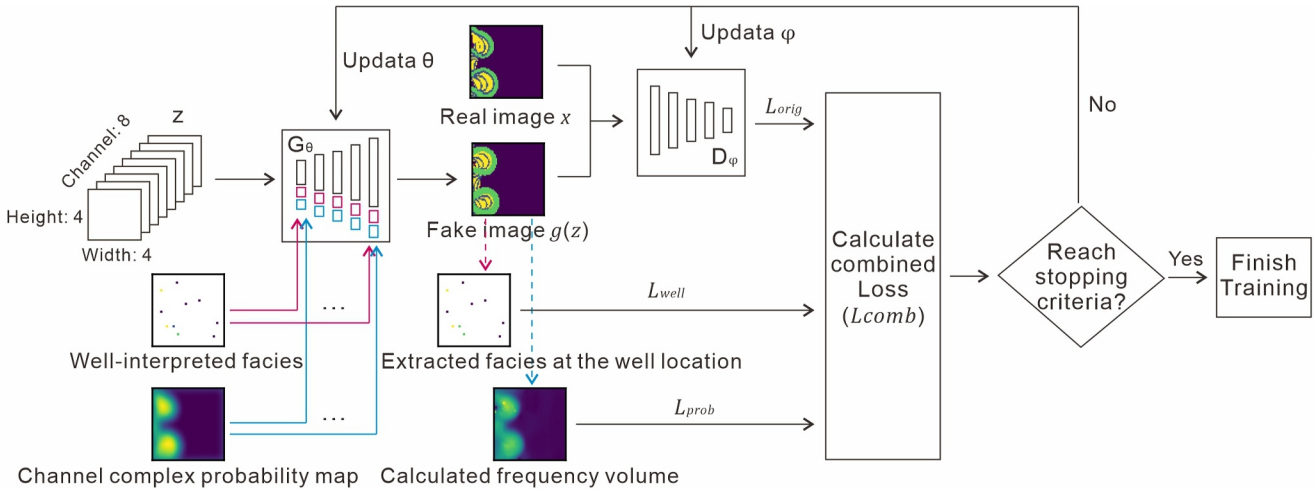

Figure 3. Schematic representation of the conditional generative adversarial networks used in the application example shown below. The generator has as inputs the latent vector, well-interpreted facies data, and probability map into the generator to generate geological realizations. Facies are extracted at the well location, and frequency volume is computed from these realizations. Loss functions—facies-pattern-based ($L(D_\varphi, G_\theta)_{\text{orig}}$: distance between fake and real images), well-based ($L(G_\theta)_{\text{well}}$: distance between extracted and input well-interpreted facies data), and the probability-based ($L(G_\theta)_{\text{prob}}$: distance between the frequency volume and input probability map)—update generator and discriminator network parameters. The channel complex probability map indicates the probability of channel development, incorporating mud drapes (blue), channel fill (green), and point bar sand facies (yellow).

3. Construction of Mud Drapes Conceptual Geomodels and Training Data Set

In this section, we generate numerous large-size conceptual facies models of modern fluvial point bars with improved ALLUVSIM. These conceptual facies models are essentially a database of geological patterns, which serve as the foundation for creating training data sets for GANs.

3.1. Modern Point Bar Examples

Figure 4 displays the meandering fluvial patterns observed in the Oulankajoki River, Rio Pardo, Likouala Aux Herbes River, and Huihe River, respectively. While high-resolution satellite imagery aids in constructing large-scale training data sets like river deltas (Nesvold & Mukerji, 2021), the thin nature of mud-drape deposits prevents their direct extraction from Earth observation data. Consequently, we indirectly identify possible mud drapes by observing variations in the direction of point bar migration (i.e., tracing past channel migrations (Russell et al., 2018)). The planform geomorphology of mud drapes, as depicted in Figure 4, hinges on channel sinuosity,

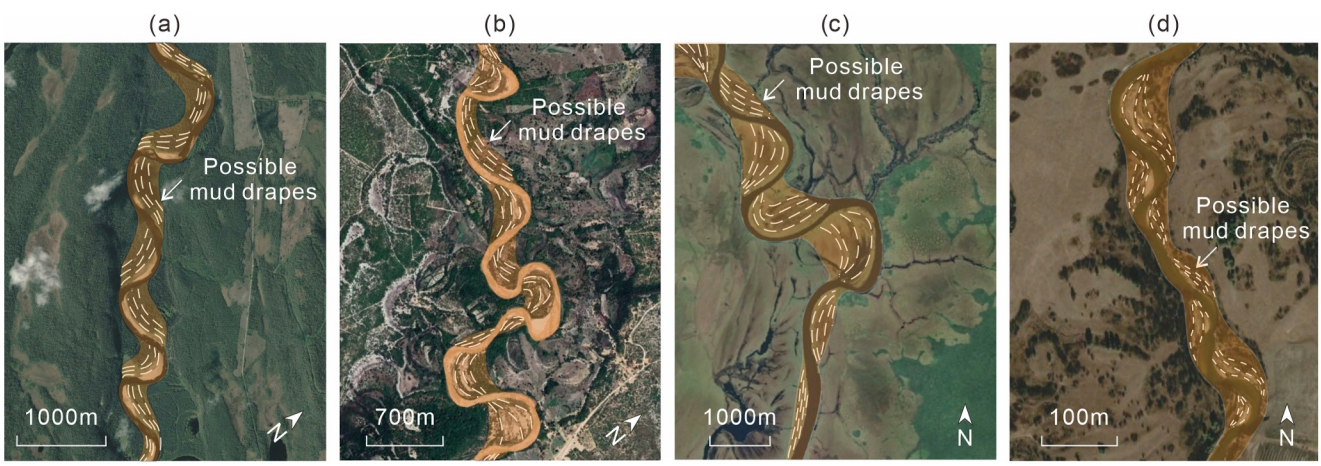

Figure 4. Four small sections of the modern rivers: (a) The Oulankajoki River, Finland (66°18′ N, 29°33′ E), (b) Rio Pardo, Brazil (15°41′ S, 44°53′ W), (c) Likouala Aux Herbes River, Congo (0°28′ S, 17°25′ E), and (d) The Huihe River, China (48°3′ N, 119°46′ E). The yellow areas represent the channels, and the white dashed lines represent the possible mud drapes.

Table 2
The Key Input Parameters for Improved ALLUVSIM

Key input parameters	Value
The simulated area (cells)	200 × 200 × 160
Grid size (m)	10 × 10 × 0.1
The target net-to-gross ratio	0.15–0.3
Orientation (°)	[0, 2] deviating from north-south direction
The average total flow in the channel Q (m^3/s)	[2, 0.5]
Step (m)	5–15
Depth (m)	1
Width-to-depth ratio	15–55
Initial channel sinuosity	[1.2, 0.05]
Sinuosity target	[1.7, 0.05]
The extension length ratio of mud drapes	[0.67, 0.1]
The frequency of mud drapes (counts)	[1–6]

Note. [a, b] represents a Gaussian distribution with mean of "a" and variance of "b", while [c, d] represents a uniform distribution ranging from minimum value "c" to maximum value "d."

wavelength, amplitude, and migration patterns. For example, the Oulankajoki River section, characterized by a low sinuosity and downstream sweep, produces nearly parallel mud drapes formations (Figure 4a). In contrast, the Rio Pardo section, marked by substantial lateral channel migration and higher sinuosity, generates crescent-shaped mud drapes formations (Figure 4b).

3.2. Construct and Validate Conceptual Facies Geomodels of Mud Drapes

In our experiment, the improved ALLUVSIM algorithm considers the genetics, shape, and sinuosity of mud drapes in meandering rivers. Table 2 summarizes the input parameters for generating two hundred 3-D realizations (Figure 5), with a grid size of 10 m × 10 m × 0.1 m, accounting for grid count, point bar characteristics, and dynamic simulation (Supporting Information S1). These realizations serve as conceptual geological facies models, providing a valuable database of geological patterns (Al-Khalifa et al., 2007; Hoffimann et al., 2021; Song, Mukerji, Hou and Zhang, et al., 2022). The preserved mud drapes' extension length ratio was approximately 0.67 from the real world (Labrecque et al., 2011; Niu et al., 2021; Yan et al., 2017). Factors like channel width, wavelength, amplitude, and migration patterns significantly impact mud drapes morphology in surface patterns, controlled by specific parameters in Table 2: Channel width relies on depth and width-to-depth ratio; "Step" determines wavelength (smaller steps result in shorter wavelengths), while channel fill sinuosity influences amplitude; "Q" affects lateral and downstream channel migration, with smaller values implying stronger lateral migration and larger values indicating stronger downstream migration. The generation process took roughly 10 hr on a standard laptop with a Core i7-10875H, 2.30 GHz CPU, and 32 GB RAM (the same computing environment used for history matching in Section 6.1).

We derived 2-D sections from the 3-D conceptual models for practical application in contemporary rivers. These images display various channel characteristics: narrow (Figure 6a) and wide channels (Figure 6d), low-sinuosity (Figure 6h) and high-sinuosity channels (Figure 6c), isolated (Figures 6a–6d, 6g, and 6h) and stacked channels (Figure 6e), asymmetrical (Figure 6a) and symmetrical mud drapes (Figure 6b), and more. The comparison between conceptual models and modern rivers revealed analogous mud-drape patterns between Figures 6a–6d and 4a–4d, respectively. These findings suggest that our mud drapes conceptual models offer promising applications in real-world scenarios.

3.3. Construction of the Training Data Sets

We consider two distinct 2-D data sets for generating unconditional and conditional facies realizations. For the unconditional simulation of mud drapes, we randomly cropped each conceptual model (200 × 200 pixels) to generate 125 2-D patches (64 × 64 pixels images). This process resulted in a total of 25,000 2-D facies models. To

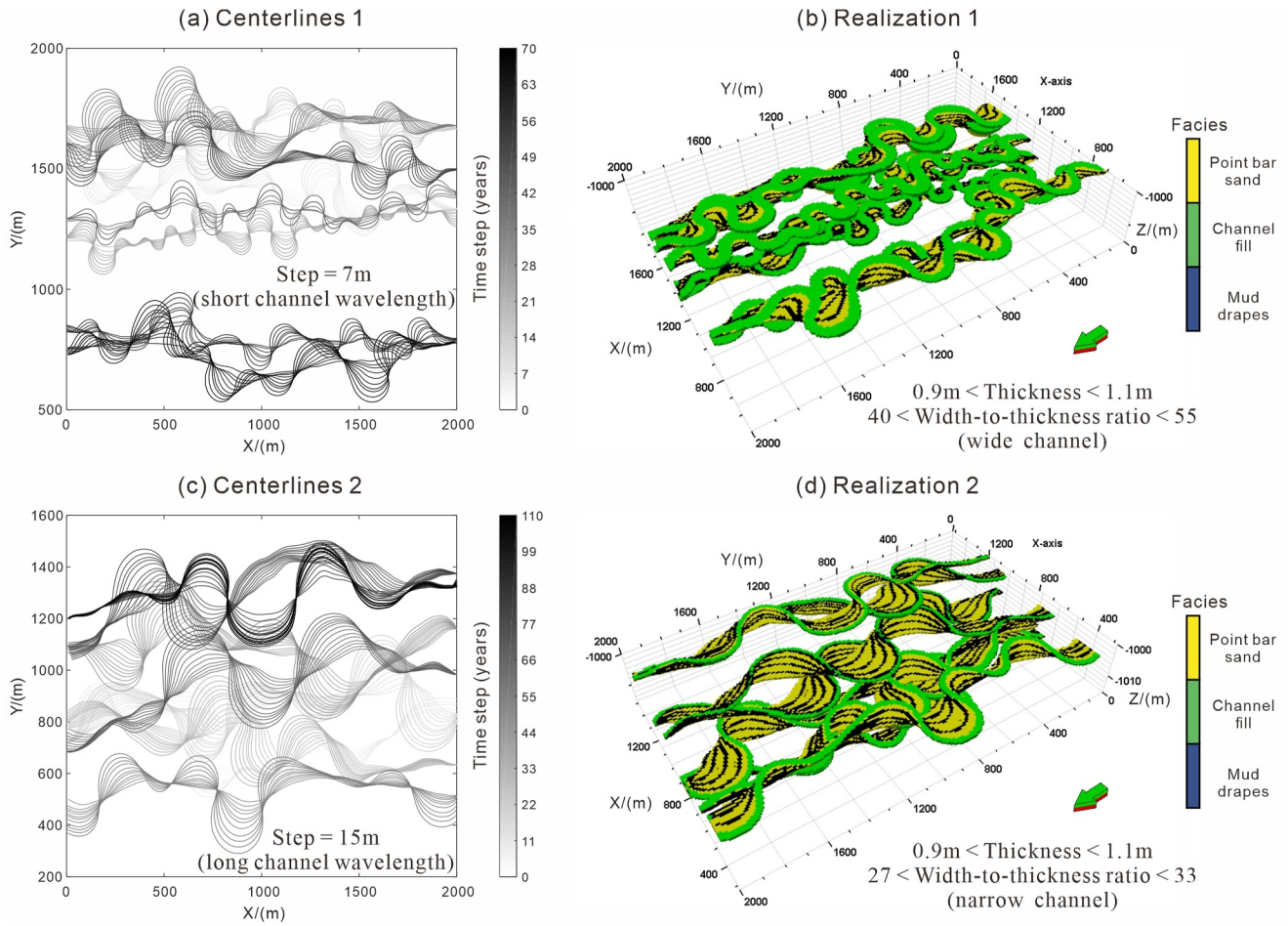

Figure 5. Two migration centerlines over several time steps (white to black) and corresponding realizations (out of the ensemble of 200 realizations) of facies models considering mud drapes. Each model has 200 by 200 by 160 cells in *i*-, *j*- and *k*-directions, respectively. Each cell is 10 m (length) by 10 m (width) by 0.1 m (height). The floodplain deposit is not shown in the representation.

ensure the quality of training images, we retained only those patches with a floodplain proportion of less than 0.8, thereby balancing the training data set to avoid the influence of models with fewer mud drapes. Figure 7a displays 14 randomly selected training facies models.

In addition to the facies models, well-interpreted facies data and probability maps are created for the conditional simulation of mud drapes. The well facies data consisted of random samples spatially distributed between 1 and 300 position points in each facies model (Figure 7b). For low-resolution probability data, we convolved a 2-D Gaussian kernel with the 2-D conceptual facies models to mimic the spatial resolution obtained in conventional seismic reflection data. The kernel size ranges from 13×13 pixels to 27×27 pixels in odd increments, with standard deviations equal to the kernel size. As individual facies probability maps may be difficult to construct due to the limitation of real seismic resolutions, especially for the presence of mud drapes, a single probability map is constructed instead of four respective probability maps (Figure 7c).

These models are randomly divided into a training data set (20,000 models) and a testing data set (5,000 models) for both conditional and unconditional cases. The training data set was used to train the generator, while the testing data set served exclusively for evaluation purposes.

4. Unconditional Geomodeling of Point Bar Architectures

We evaluated the results from the trained unconditional generator by comparing the produced models with those obtained from MPS through visual inspection, two-order and high-order statistics.

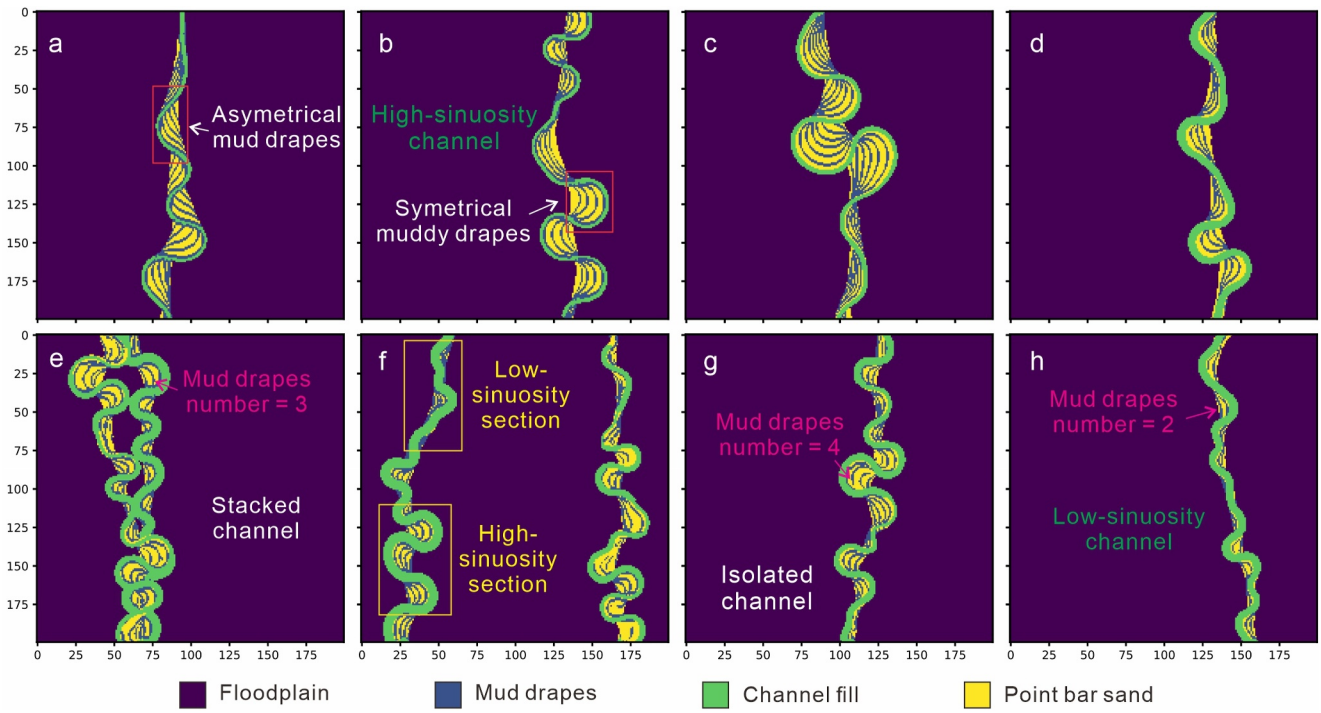

Figure 6. Eight random horizontal sections extracted from the three-dimensional realizations of mud facies models generated with improved ALLUVSIM. The 2-D image axis unit here and hereafter is pixels, not the actual distance.

4.1. Training of the Unconditional GAN

Training is performed on the TensorFlow platform and in parallel using two NVIDIA Tesla V100 GPUs. The specific hyperparameters for the GAN are summarized in Table 3. The quality of the generated models is evaluated using SWD-MDS after each batch. Visual inspection serves as the primary criterion for stopping the training process. The training process takes approximately 17 hr, reaching a training epoch of 7,000. We decided to use a large number of epochs to ensure convergence during training.

4.2. Evaluation of the Trained Generator

Figure 8 shows multiple realizations generated from the unconditional MPS (i.e., DeeSse) (Mariethoz et al., 2010, 2015; Straubhaar et al., 2020) and the proposed GAN architectures. A visual inspection reveals that the unconditional GAN produces, for the different facies, spatial patterns that agree with real sedimentary and the corresponding conceptual geomodels (Figures 4 and 6, respectively). The reproduction of sedimentary features includes continuous, curvilinear channel fills, complete point bars on the convex bank of channel fill, and continuous curvilinear mud drapes inside point bars; on the contrary, MPS-produced results show many severely unrealistic features (e.g., discontinuous channel fills and mud drapes). The GAN-produced channels in different realizations present varying widths and sinuosity, resembling real depositional systems. However, some GAN-produced facies realizations have minor local noises (Figure 8), suggesting that the unconditional generator may not completely capture the spatial patterns of the training models. Continuing training and a larger, richer training data set may address that minor noise problem.

The facies-dependent average variogram models computed from the unconditional MPS and GAN realizations are shown in Figure 9. These facies-dependent NS and EW directional variogram models reveal the continuity of each facies, which decreases in the following order: floodplain; point bar sand; channel fill; mud drapes. The variogram models retrieved from the GAN realizations closely align with those from the training data, while MPS-derived models show slight deviations. Depending on the facies MPS under- or over-estimates the spatial continuity as retrieved from the training data set.

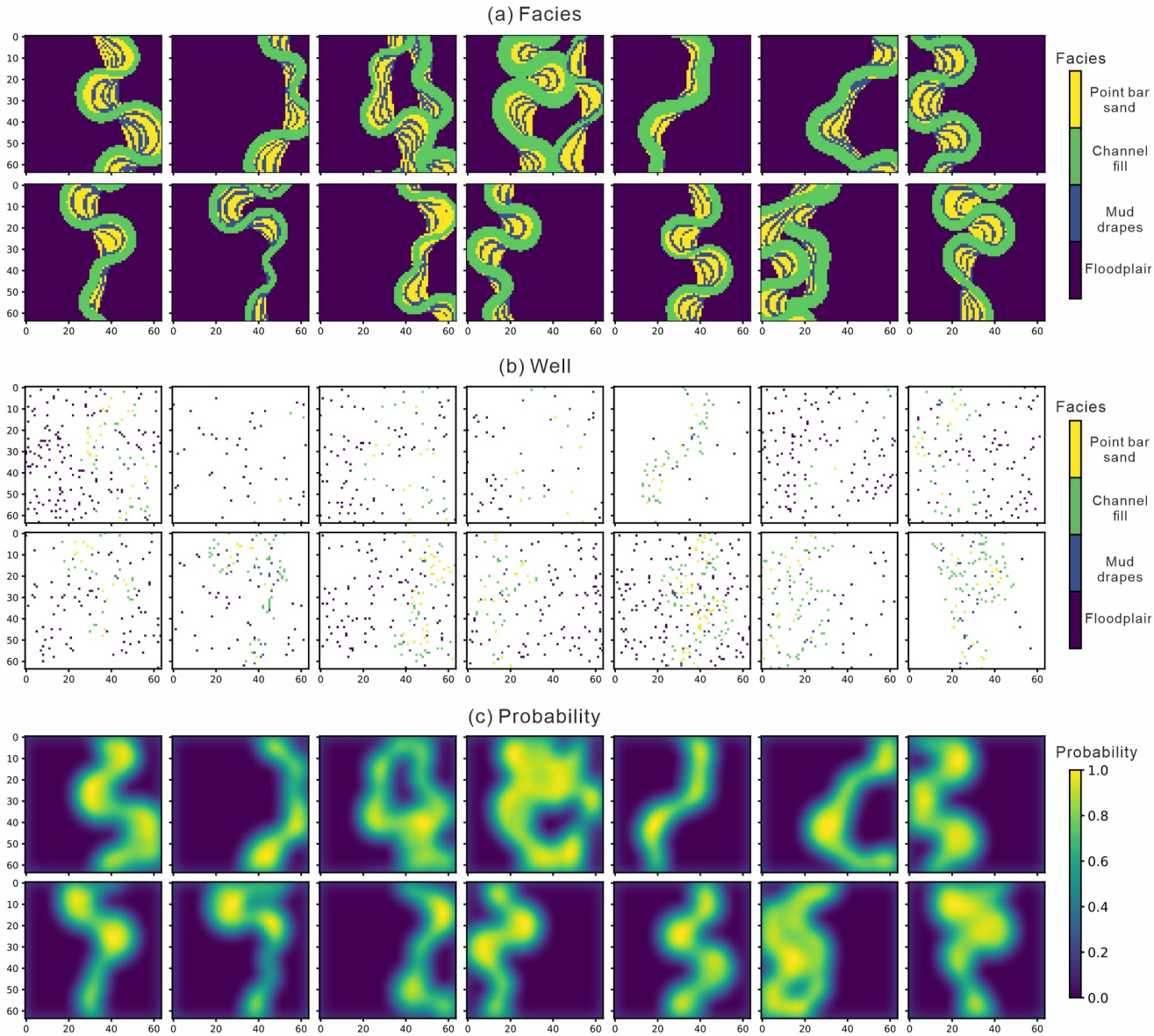

Figure 7. (a) Mud drapes models, (b) corresponding well-interpreted facies data, non-well locations were set to white for intuitive visualization of well point locations and facies types, and (c) probability maps (i.e., channel complex probability map in Figure 3) used as the unconditional and conditional training data sets (14 out of 25,000). Each model is 64 × 64 pixels.

Table 3
Hyperparameters of the Unconditional Generative Adversarial Networks

Hyperparameter	Value
Learning rate	0.0001
Beta 1	0.9
Beta 2	0.99
Epsilon	1e−8
Maximum epochs	15,000
Batch size	32

Besides, we use SWD-MDS to map 200 models from training data, 200 produced with MPS, and 200 produced with GAN. The resulting ensemble has a total of 600 points (Figure 10). The SWD-MDS's first and second components (X and Y axis of Figure 10) explain around 75% of the total variance of the data. The distribution of GAN-produced geomodels closely aligns with that of the training data set, while MPS-produced data show a slight deviation from the training data. This alignment implies that the trained generator effectively learned spatial patterns of the channel-point bar-mud drapes sedimentary system. Therefore, we can regard our trained unconditional generator as a proxy for improved ALLUVSIM.

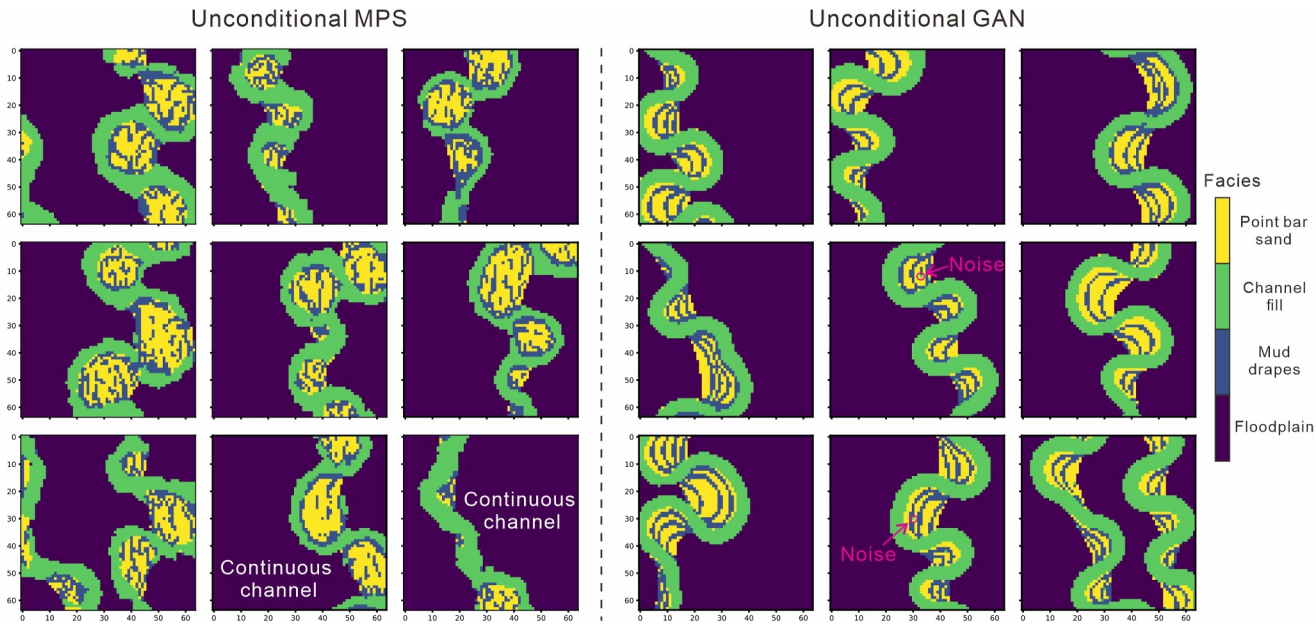

Figure 8. Unconditional facies realizations: multiple-point statistics (MPS) (left) and generative adversarial networks (GAN) (right). MPS exhibits discontinuities in mud drapes and channel fill, while GAN exhibits minor localized channel fill noise in the point bar sand.

5. Conditional Geomodeling of Point Bar Architectures

In this application example, well-interpreted facies data and probability maps are added to the generator as conditioning data (Section 2.3).

5.1. Training of Conditional GAN

The same configuration in terms of computational resources and hyperparameters used to train the unconditional GAN was used herein. Besides, we select a relatively suitable weight of various loss functions ($\beta_{\text{orig}} = 1$, $\beta_{\text{well}} = 0.25$, and $\beta_{\text{prob}} = 0.15$) to assess the conditioning ability and have facies pattern distribution with the training data set. These weights were set after trial and error. Despite the additional input data, the training phase of the GAN was no impact as it took us about 17hr to complete it.

5.2. Evaluation of the Trained Generator

In the test data set, we randomly selected eight groups of reference facies models, associated well-interpreted facies data, and probability maps for conditional testing (Figure 11). Note that the probability map can directly be used as conditioning GAN input, while we need to divide probability into four facies probabilities for MPS simulation. Assume that P_{lp1} represent the probability map and $P_{gp1}(\cdot)$ represent the global proportion of corresponding facies in case 1. We set the probability map of floodplain $1 - P_{lp1}$, and the probability map of point bar sand is $\frac{P_{lp1} \cdot P_{gp1}(\text{point bar sand})}{(P_{gp1}(\text{mud drapes}) + P_{gp1}(\text{channel fill}) + P_{gp1}(\text{point bar sand}))}$. These selected groups included various scenarios such as a high-sinuosity channel (e.g., case 1 in Figure 11) and stacked channels (e.g., case 4 and case 6 in Figure 11). As expected, due to the constraints of well-interpreted facies data and probability map, the conditional realizations' spatial variability is smaller than the corresponding unconditional realizations. Generating geologically plausible mud drapes using conditional MPS proved difficult. However, the realizations generated from conditional GAN exhibit a high-level of realism and closely resemble the associated reference models.

Figures 12 and 13 assess the degree of matching between the observed data and 10,000 facies models generated by conditional GAN in each case. Around 80% of realizations precisely match corresponding well-interpreted facies data at 100% (Figure 12), while the frequency density distribution of channel complexes matches respective

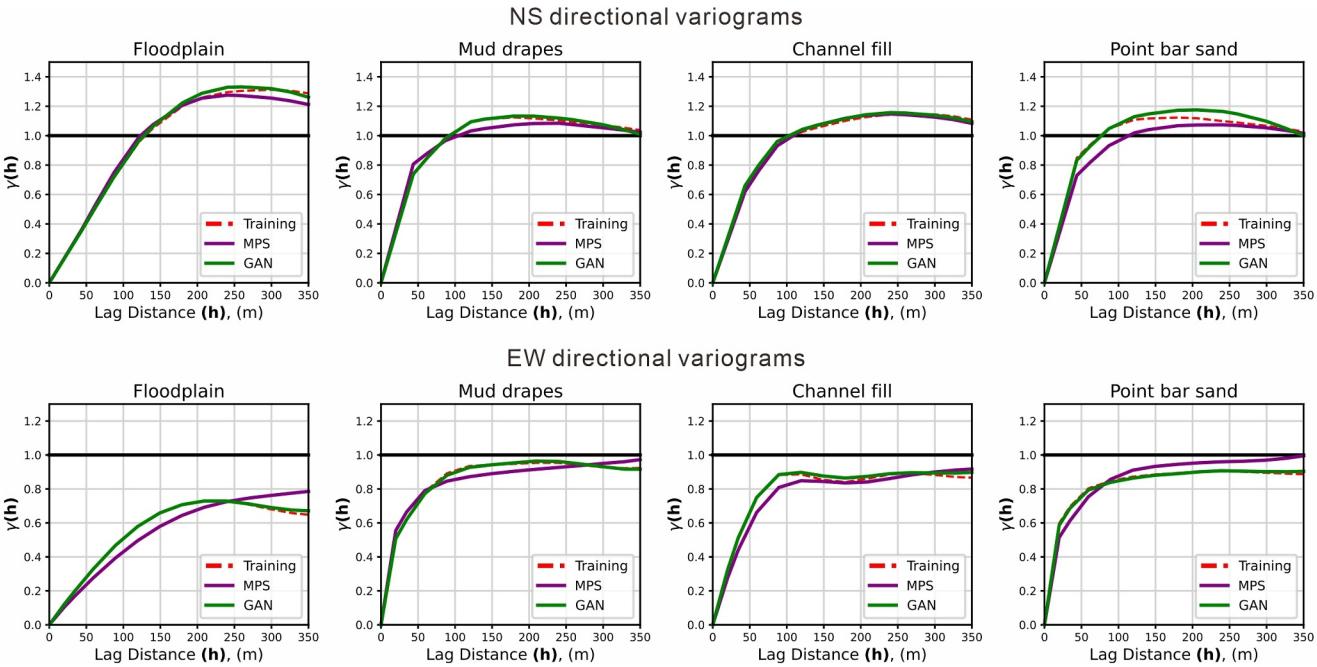

Figure 9. Comparison of the average variograms models from 200 training (red), 200 MPS-produced (purple), and 200 GAN-produced geomodels (green) in the NS and EW directions.

probability maps (Figure 13). Despite close matches to observed data, these generated models exhibit significant diversity.

Figures 14 and 15 focus on case 8 (Figure 11) to assess the diversity and similarity within the generated realizations from the trained conditional generator. In this example, wells W1, W2, and W3 are located within the same single point bar in the reference facies model. However, in realization *b* of Figure 14, wells W1 and W2 share the same single point bar but differ from well W3; Furthermore, Wells W1 and W2 are connected by point bar sand in the reference facies model, whereas they are blocked by a mud drape in realizations *c* and *i* in Figure 14. Additionally, 2-D projections from SWD-MDS (Figure 15) show that the reference case 8 distributions are inside the conditional GAN data distributions, and the data distributions themselves are almost encompassed

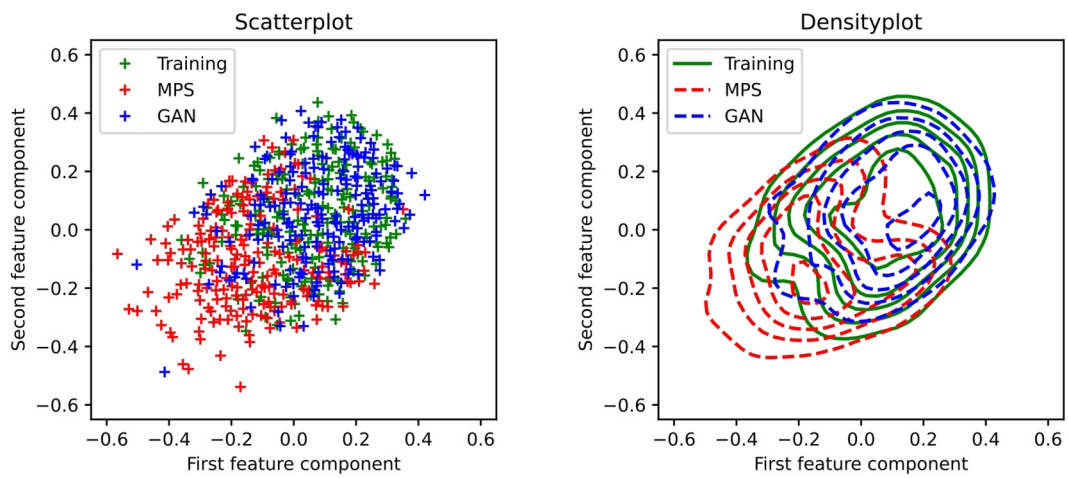

Figure 10. The sliced Wasserstein distance and multidimensional scaling visualization of the distribution of the training data (green), unconditional multiple-point statistics data (red), and unconditional generative adversarial networks data (blue) in 2-D space. The left is a scatter plot, while the right is a density plot calculated from the left with the Gaussian kernel method.

10.1029/2023WR035989

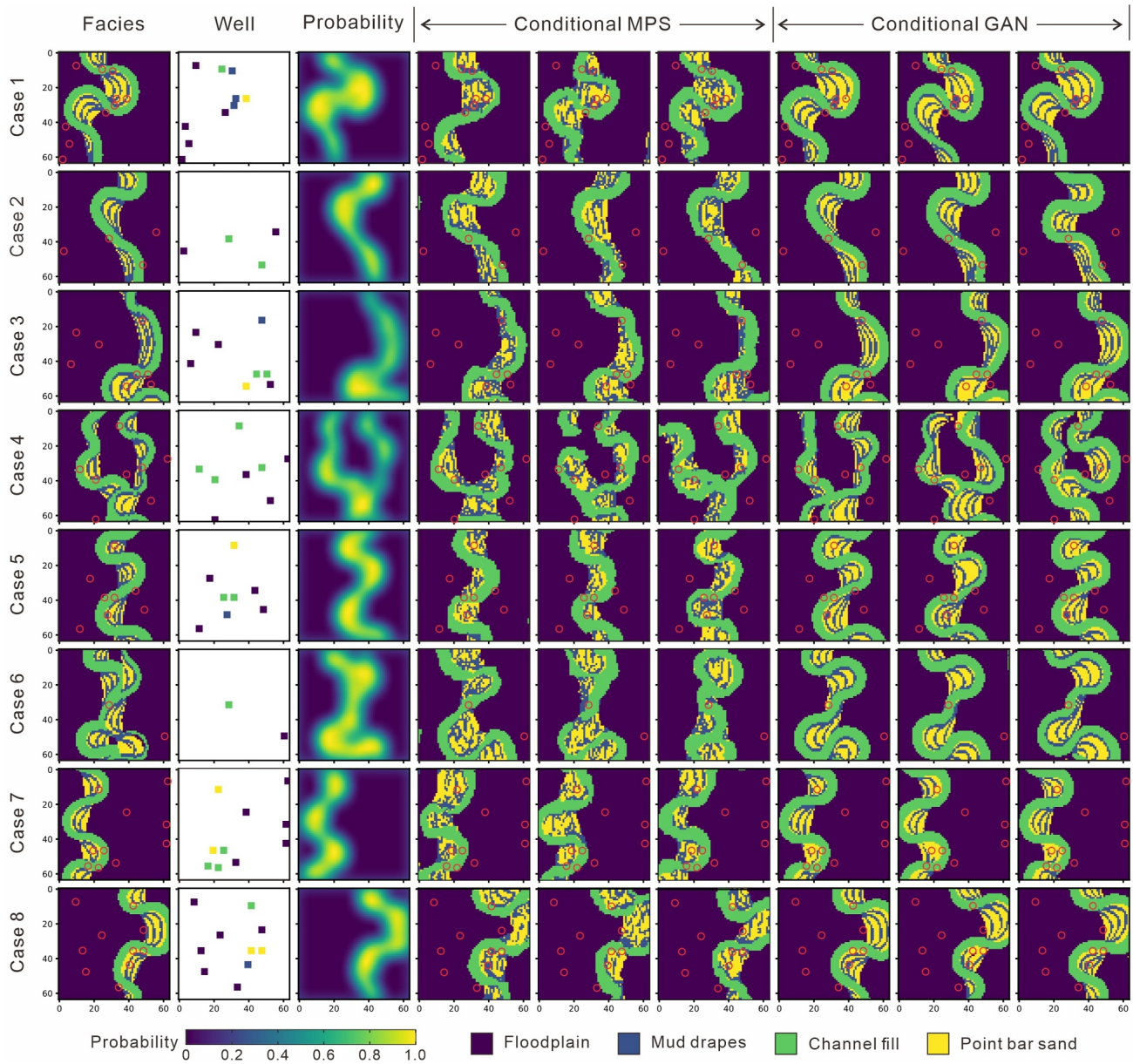

Figure 11. Columns one to three display reference facies models, well-interpreted facies data, and (channel complex) probability maps, respectively. Columns four to six show multiple-point statistics (MPS) realizations and the remaining columns show generative adversarial networks (GAN) realizations. Red boxes in both reference and generated models indicate the location of conditional well-interpreted facies data. Both MPS and GAN simulation results match well-interpreted facies data.

within the distribution of the training data. Hence, the conditionally trained generator possesses robust capabilities in extracting mud-drape features, performing data conditioning, and producing multiple diverse realizations.

6. History Matching Using the Pre-Trained Generator

This application example has three objectives: clarify the barrier effect of mud drapes on fluid flow through forward BHP numerical simulation; verify that the conditional pre-trained generator can be applied to modern meandering river applications through high-order statistics and dynamic history matching; and reduce the uncertainty associated with the prediction of mud drapes from BHP inversion.

The high-resolution Google Earth satellite image in Figure 16a depicts modern point bars from the Lalin River in China. Within the channel bars, possible mud drapes were manually marked with purple, blue, and red solid lines.

10.1029/2023WR035989

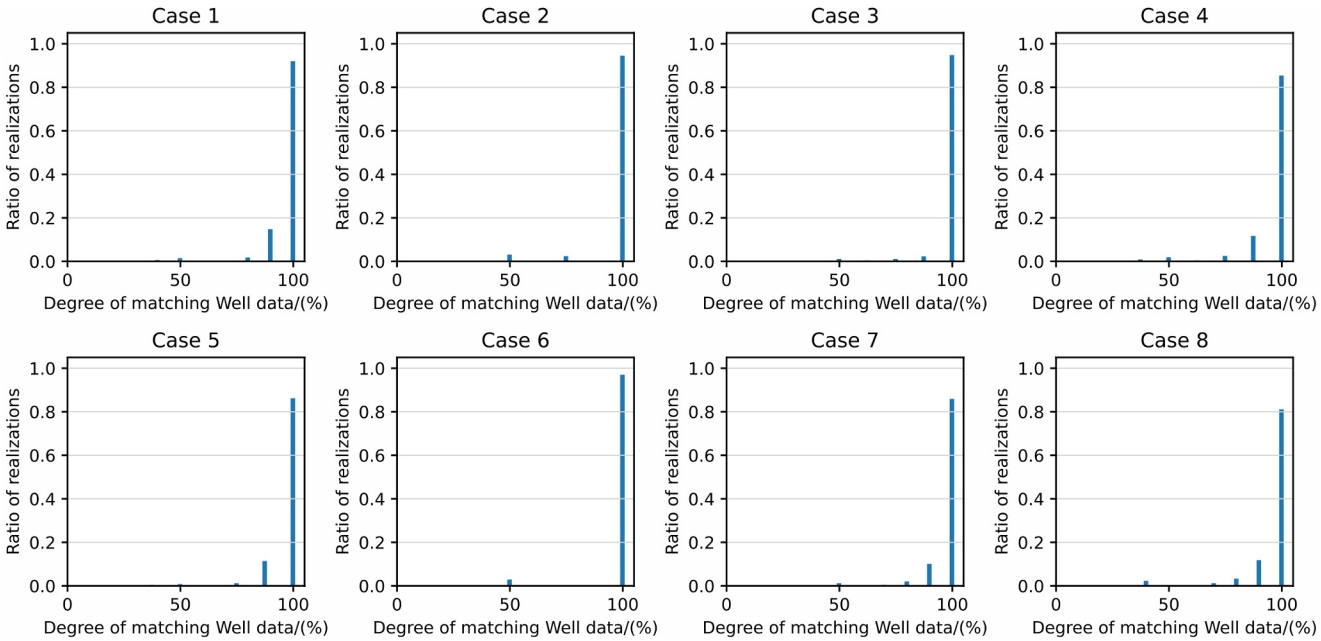

Figure 12. The ability of conditional generative adversarial networks to condition well-interpreted facies data of all cases in Figure 11.

To address scale differences between real Google images and our synthetic training data set, we preprocessed the training data to align the scaled training models' channel width with that of the modern rivers. The synthetic training data's channel width (ranging between 14 and 48 m) was adjusted to match the surface channel width range in the ground case (between 13 and 19 m) by reducing the training data size to 0.86 times. This adjustment resulted in a training data channel width ranging between 12.9 and 47.3 m, covering the ground case channel width. Thus, the synthetic grid size became 8.6 m × 8.6 m, and the simulated areas can be divided into 64 × 64 grids (Table 4). Next, we converted this Google image to the corresponding reference facies model (Figure 16b) and selected eight random positions as reference (observed) well-interpreted facies data (Figure 16c). The

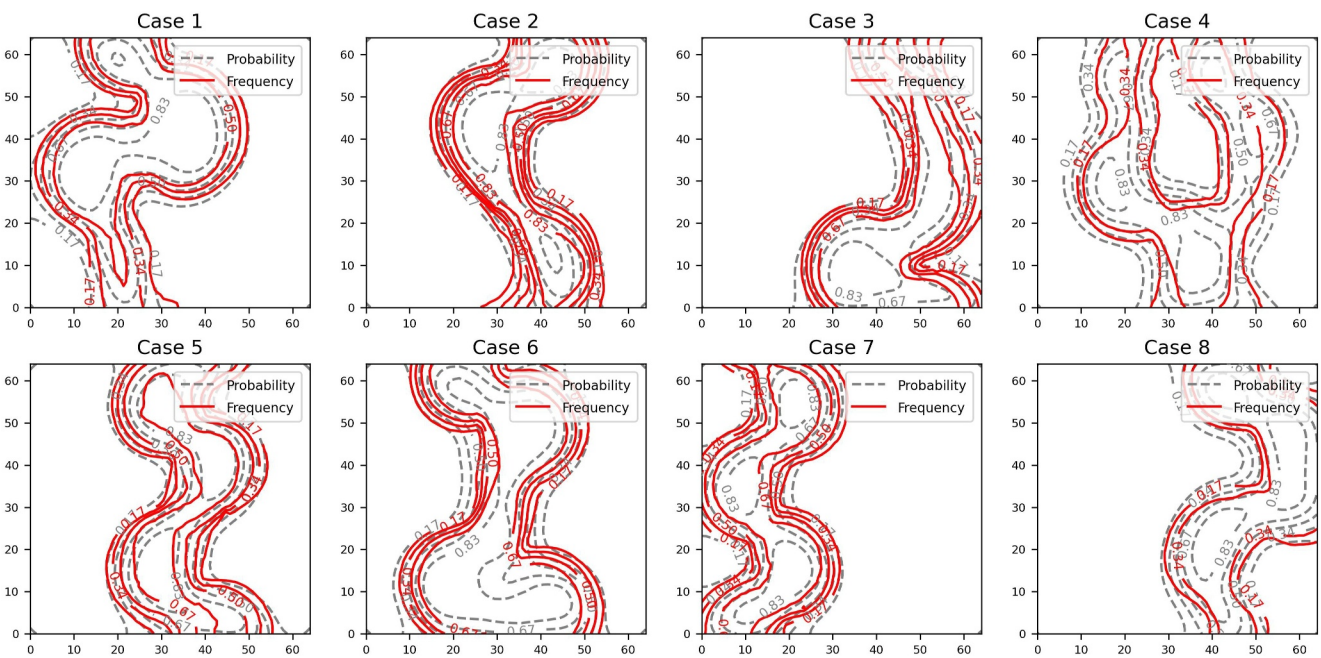

Figure 13. Contour plots of probability (gray dashed lines) and frequency density (solid red line) of all cases in Figure 11.

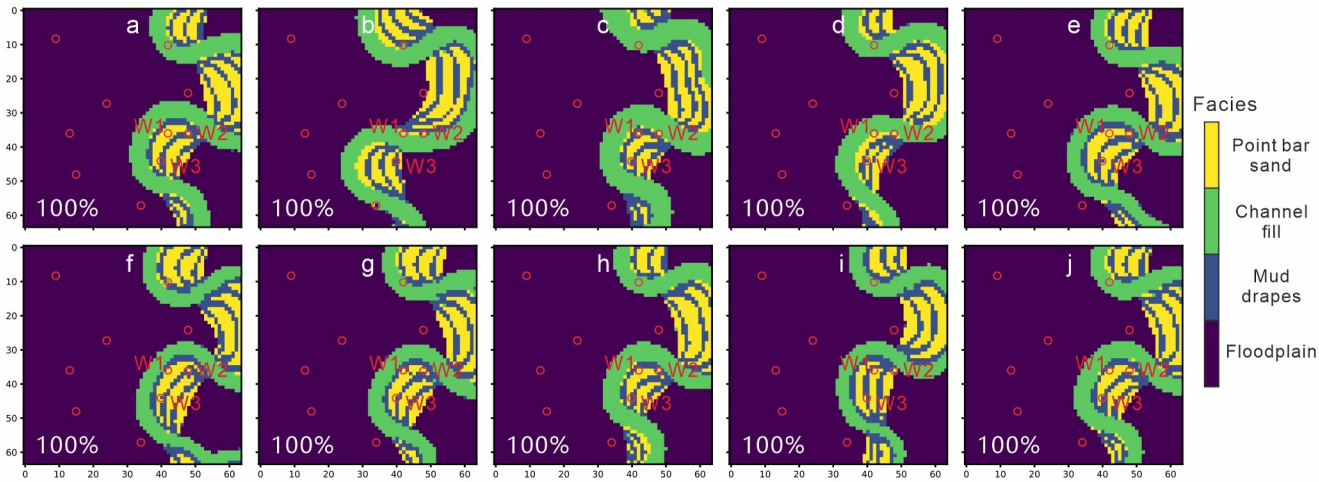

Figure 14. Ten conditional GAN-produced facies realizations in Figure 11's case 8, showcasing precise matches with well-interpreted facies data at 100%. The choice of three closely spaced wells (W1, W2, and W3) enables detailed observation of subtle differences within each generated realization.

probability map (Figure 16d) was obtained by convolving the reference facies model with the convolutional kernel of size 13 × 13. Additionally, using a numerical fluid flow simulator, we simulated steady-state groundwater flow transport from north to south through the reference facies model. BHP values were measured over a period of 50 days at eight wells, providing reference (observed) BPH data (Figure 16e). The upper and lower pressures were fixed at 344 and 329 bar, respectively, with impermeable left and right boundaries. We assumed constant hydraulic conductivity within the same facies, as groundwater flow is typically constrained by facies type (Table 5).

Figure 17 shows forward BHP numerical simulation of reference channels with and without mud drapes at different intervals. The results demonstrated that the pressure models of the mud-drape-free channel (100% sandstone within the point bar) remained essentially unchanged after day 5. In contrast, the pressure models of the reference channel with mud drapes underwent significant changes within 15 days, indicating the crucial role of mud drapes in impeding fluid movement and interrupting connectivity in sandy point bar reservoirs.

Next, by inputting random latent vectors, well-interpreted facies data and probability maps into the pre-trained generator, multiple facies realizations were generated. However, the pre-trained conditional generator occasionally produces realizations that do not perfectly match the conditioning hard data (Figure 12). To ensure accuracy in matching well-interpreted facies data, a fast evaluation is performed. The ensemble of these fast-evaluated realizations represents the prior space. Figure 18 displays multiple prior facies, resembling the reference facies model. SWD-MDS plots (Figure 19) illustrate the relationships among reference facies data (black), the training data (green), corresponding prior data (blue), and corresponding posterior data (red) in 2-D space. The distribution of the reference data is projected within the distribution of the prior data, while the prior data distribution is projected within the distribution of the training data, suggesting consistency between mud-drape patterns from the surface meandering river and synthetic mud-drape patterns from the training data set. Furthermore, the true BHP curves are within the range of BHP curves produced by these facies realizations (Figure 20). However, the mean and variance maps of 1,200 prior facies models indicate high uncertainty of mud drapes inside point bars (Figure 21).

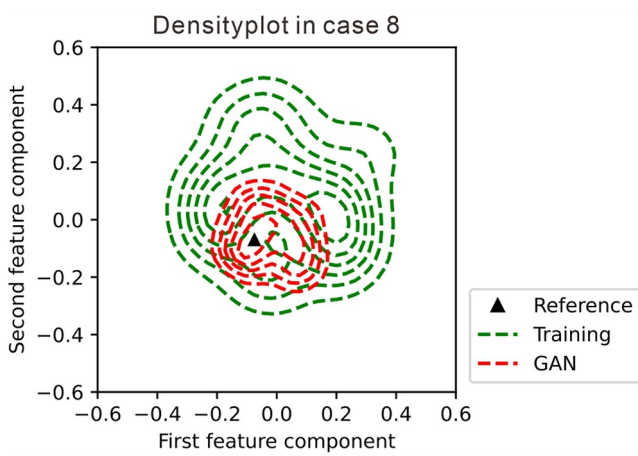

Figure 15. The sliced Wasserstein distance and multidimensional scaling visualization of case 8 in Figure 11. The relationship between the reference data (black), 50 training data (green), and conditional GAN-produced data (red) in 2-D space.

We then applied McMC-based history matching to perturb the facies generation to reproduce the observed BHP data. Figure 22 shows results from rejection and McMC. Rejection sampling accepts a suggested model based on

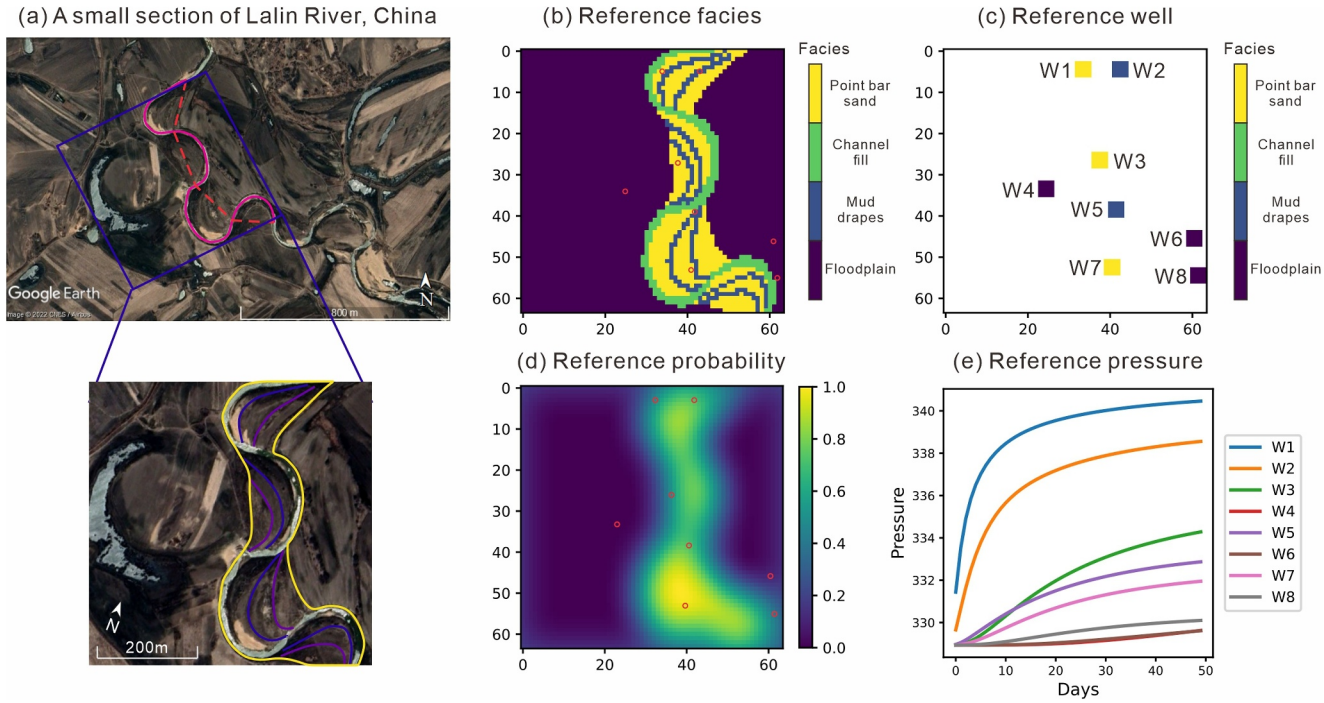

Figure 16. (a) Selected area in the Lalin River, China (45°24′ N, 125°40′ E), outlined by the blue box, showcasing a 782 m channel bed (red dotted line) and a 1,381 m channel fill (solid pink line) with a sinuosity of 1.77. The yellow solid line outlines the channel's contour within this selected area, representing approximately 25.6% of the total area (net-to-gross ratio). Purple and blue solid lines inside point bars indicate possible mud drapes formed during channel migration. (b–e) display the reference facies model, well facies, probability map, and bottomhole pressure curves, respectively.

its likelihood function ratio to the maximum likelihood function of all models, that is, $L(m^i|d)/L_{\max}(m|d)$ (Jeong et al., 2017). Despite both methods yielding a root mean squared error (RMSE, the square root of $F(m)$ in Equation 3) of approximately 0.75, rejection sampling shows a mere 0.16% model acceptance rate, contrasting with McMC's 3.06% rate. Since 5,000 evaluations take around 14 hr, higher acceptance will significantly reduce computational costs. Strategies like integrating simulated annealing can further increase acceptance rates. Typically, an acceptance rate of 25%–50% for suggested models is considered computationally efficient (Gelman et al., 1996; Hu et al., 2023; Laloy et al., 2016). After a burn-in period of approximately 1,400 iterations, posterior models were sampled. Six Markov chains are obtained for the ground case. The mean and variance maps for each facies type of the posterior models were derived from 1,200 models, selecting every eighteenth facies model from the last 3,600 iterations of each chain. The results demonstrated that incorporating dynamic data reduced facies distribution uncertainty, particularly regarding mud drapes (Figure 21). Additionally, the posterior data distribution is projected within the prior data distribution in the SWD-MDS plot (Figure 19), and the pressure of both reference and inverted models at eight wells fit more closely than the pressure of prior models (Figure 20), both indicating a further reduction in mud drapes uncertainty through BHP inversion. Thus, the proposed workflow provides technical support for predicting reliable mud drapes distributions in real-world scenarios, which could be a great help in the uncertainty prediction of subsurface water flow, contamination mitigation, geological storage of CO_2, and exploitation of oil and gas.

Table 4
Channels Parameters

Case	Channel width (m)	Sinuosity	Scaling	Grid size (m^2)	Cells number	Area (m^2)
Training data	15–55	1.5–1.9	\	10 × 10	64–64	640 × 640
Ground case	13–19	1.77	0.86	8.6 × 8.6	64–64	550 × 550

Table 5
The Hydraulic Conductivity Value in Each Facies

Facies type	The hydraulic conductivity values
Point bar sand	2,233 md
Channel fill	1,624 md
Mud drapes	8 md
Floodplain	5 md

7. Discussion

The proposed geo-modeling workflow uses improved ALLUVSIM to produce realistic and high-resolution models of fine-scale mud drapes inside point bars. While satellite images (e.g., Google Earth™) are readily available and offer realistic geologic patterns, they often lack the resolution necessary to accurately identify small-scale mud drapes within point bars and are 2-D. In the proposed geo-modeling workflow, a process-mimicking-based method serves as a substitute for satellite images in generating realistic training data. Improved ALLUNSIM produces 3-D conceptual facies models of mud drapes that closely resemble the architectural geological elements of real-world fluvial point bars. Other methods, such as the Point-Bar Sedimentary Architecture Numerical Deduction (PB-SAND) (Yan et al., 2017) which uses time series of central curves of shifting meandering channels to build inner architecture point bar deposits as well as digitalization of flume experiment results, also aids in constructing realistic mud drapes models. These models are suitable for training GANim, and the trained generator can be used to generate multiple stochastic realization that reproduce complex sedimentary patterns considering various types of conditioning data (e.g., point data and probability maps). The introduction of conditioning data does not increase the computational costs or degrades the quality of the predictions. The proposed GANim architecture performs better than geostatistical methods including the MPS-based approaches. Other generative models (e.g., diffusion models (Ho et al., 2020) and variational autoencoders) suitable for pattern reproduction and conditional simulation can be potential substitutes for GANSim models.

The quality of simulated mud drapes models from the pre-trained generator heavily relies on the quality of the training data sets. This paper focuses on two types of mud drapes: some spanning the entire thickness of point bar fronts and others confined to the upper parts of point bars. However, discontinuous and irregular types were not considered (Thomas et al., 1987). Additionally, elements like oxbow lake deposits in meandering channel systems formed by repeated meander loop cut-off and the reworking of older point bar sediments were overlooked. This necessitates attention to additional channel parameters like channel abandoned frequency and channel numbers and arouses a potential requirement for the physics-based models such as improved ALLUVSIM. Moreover,

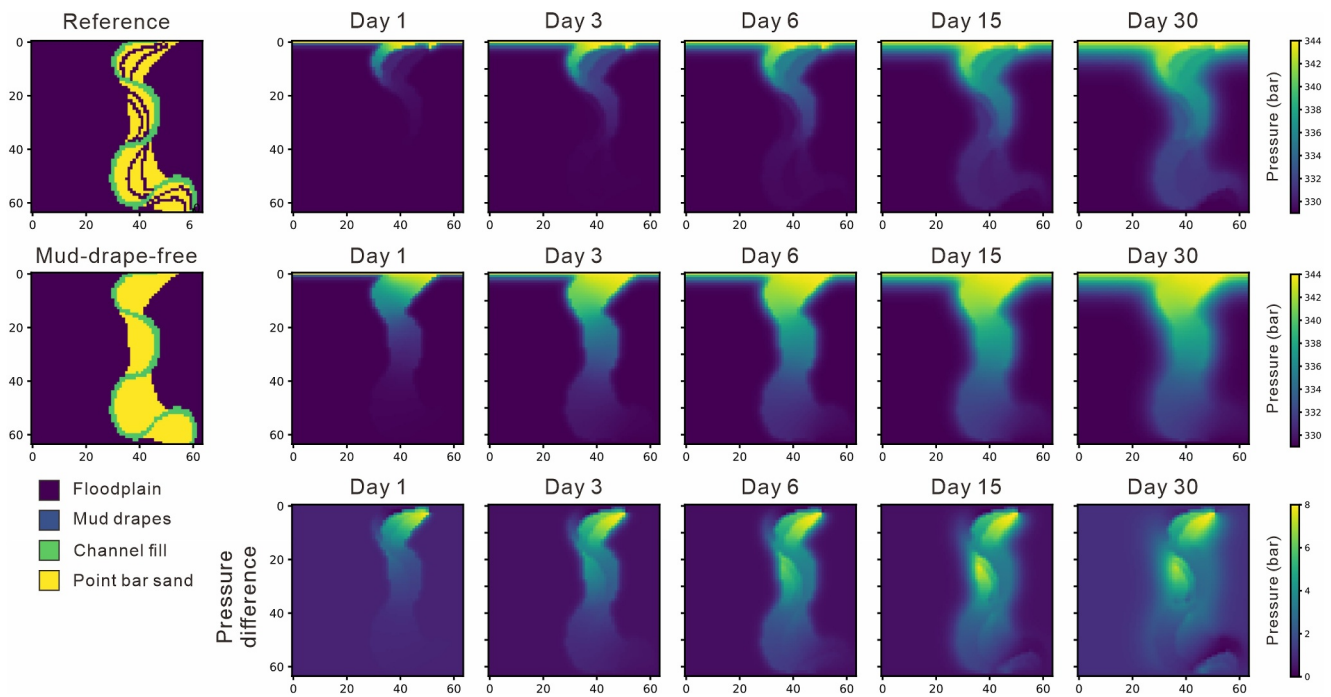

Figure 17. The first two rows show the ground case's reference models with mud drapes, and the corresponding mud-drape-free model, along with their respective pressure maps after diverse days of groundwater flow from the upper to lower boundaries. The third row displays the pressure difference between reference channels with and without mud drapes. Notably, the point bar sand exhibits a markedly larger pressure difference compared to the channel fill.

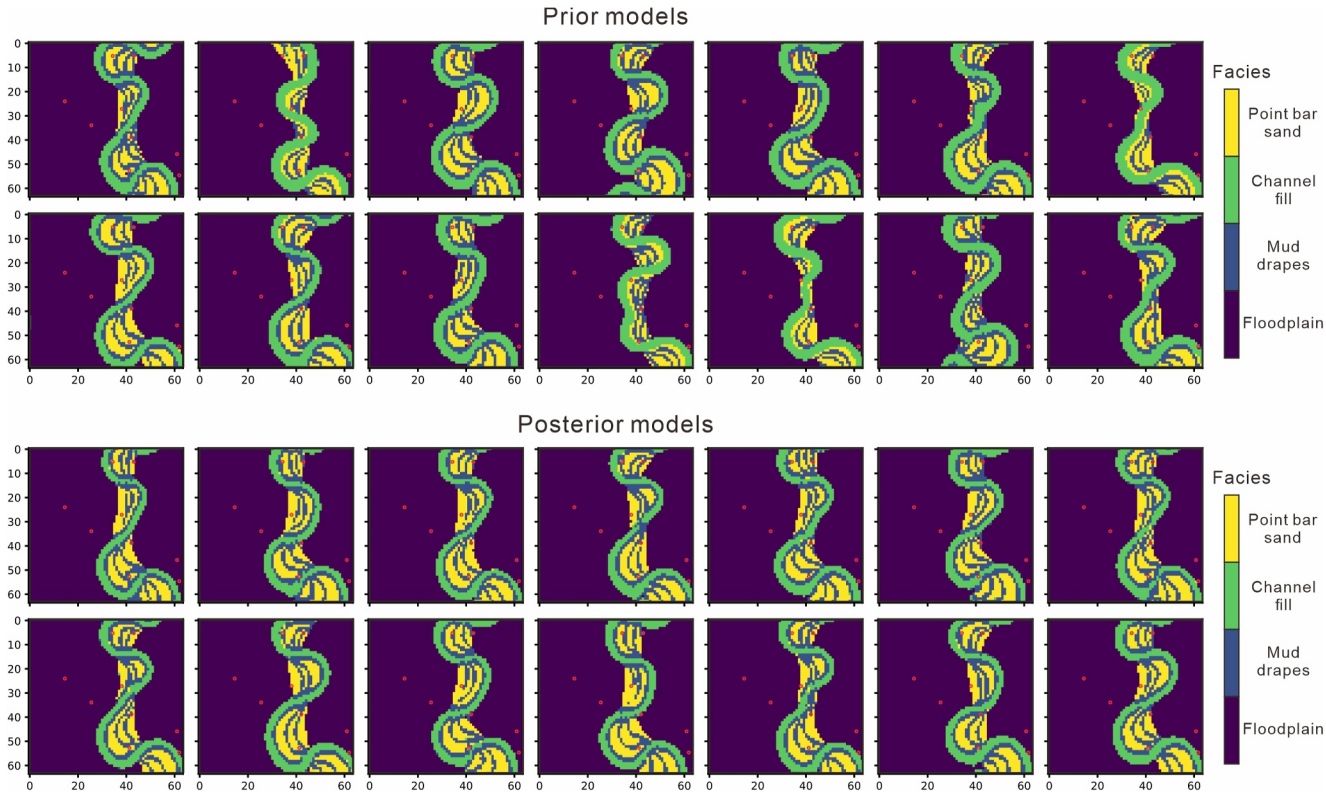

Figure 18. Prior and posterior mud drapes models in the ground case.

integrating other architectural elements, such as levees and crevasse splays, into current mud drapes models is crucial for a more comprehensive training data set.

While GANSim exhibits good performance in generating realizations that match conditional data (i.e., well and probability data), the trained conditional generator occasionally produces realizations that do not perfectly match the conditioning hard data (Figure 12). Increasing the training time may improve the match degree between simulated geomodels and the conditioning data. Thus, achieving a balance between computational cost and matching accuracy is crucial. Moreover, probability maps derived from geophysical modeling are utilized as soft

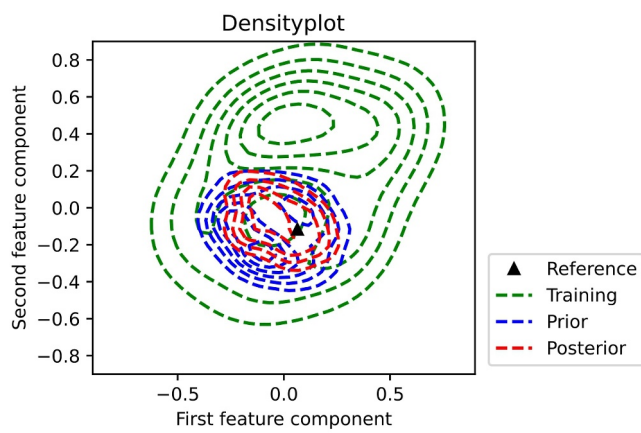

Figure 19. Sliced Wasserstein asserstein distance and multidimensional scaling visualization. The relationship between reference data (black), training data (green), corresponding prior data (blue), and corresponding posterior data (red) in 2-D space in the ground case.

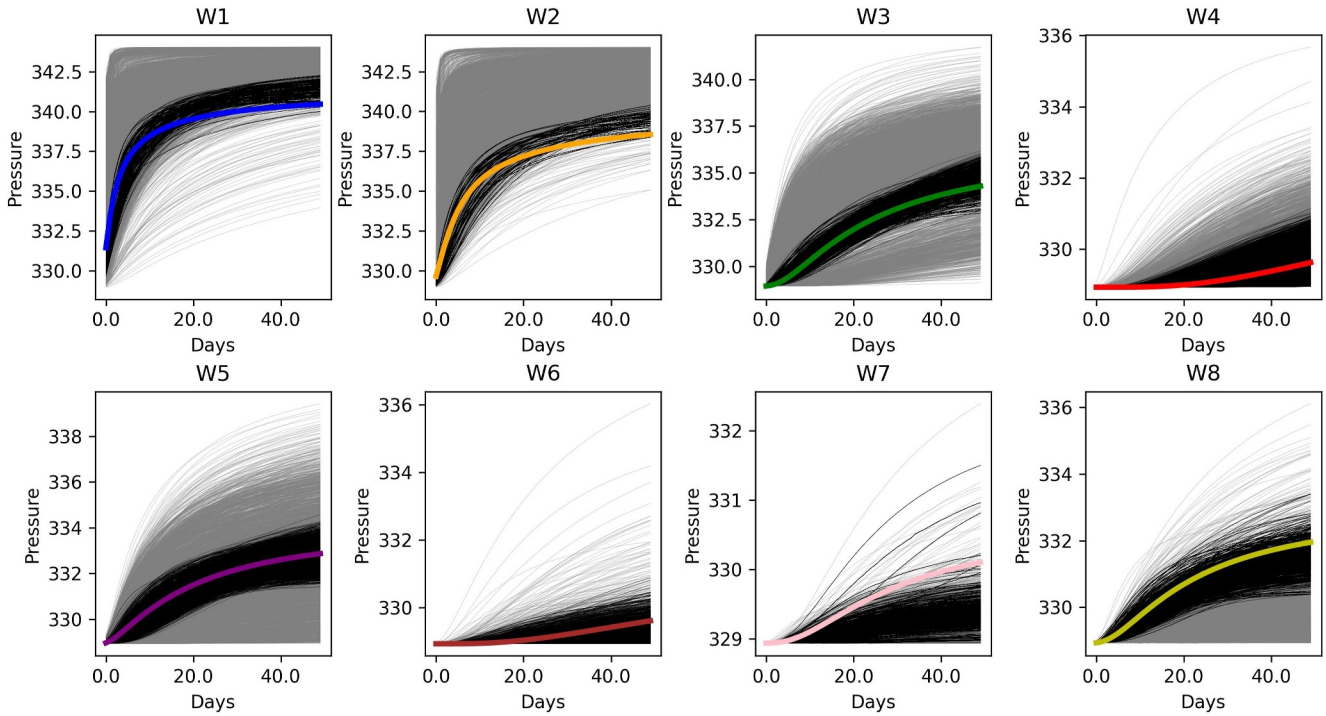

Figure 20. The bottomhole pressure curves comparison among reference (colored), prior (gray), and posterior models (black) at eight wells in the ground case. Little pressure variation, exemplified by W7, may lead to poor history matching.

data for mud drapes modeling. Due to the limitation of real seismic resolutions, one single probability map of multiple small-scale facies types (e.g., the lateral accretion and mud drape) may be interpreted instead of separate ones for each facies type. We may directly incorporate seismic data as input into the network architecture of GANSim to enable the generator to directly learn the relationship between seismic data and facies models.

A natural extension involves applying the proposed workflow to other channel sedimentary settings, such as tidal channels and deep marine channel-levee system (Li & Caers, 2011). Mud drapes features may vary across different sedimentary settings due to distinct channel patterns. For example, deep marine channel systems may exhibit more discrete (with abrupt jump) channel migrations and vertically aggradation than fluvial channel systems (Kolla et al., 2007). The proposed GAN architecture should be able to cope with such sedimentary geometries as long as they are well represented in the training data set.

Although GANSim has been utilized for 3-D geomodeling of karst caves (Song, Mukerji, Hou and Zhang, et al., 2022), that karst cave case considers binary facies types (cave vs. non-cave) and the geological features of simulated caves are relatively simpler. In this work, we have four facies types, each with different scales and geological patterns. The additional facies classes represent a challenge for the generator training. Therefore, we utilize a 2-D modern case first to validate the effectiveness of GANSim for such complex multiple-facies type cases. Challenges of shifting to 3-D GANSim include the largely increased complexity for mud-drape patterns, a largely increased requirement of computational resources, and the longer training times. Besides, selecting suitable hyperparameters (e.g., β_{orig}, β_{well}, and β_{prob} in Equation 1) could be more time-consuming. However, compared to 2-D models, 3-D geologic modeling and flow simulation will play more important role in predicting reservoir behavior because the possible absence of mud drapes at the lower part of point bars could improve the continuity of lateral accretion sand and thus result in tortuous paths of fluid flow (Li & White, 2003; Pranter et al., 2007).

We also assessed the impact of the generated facies models on the fluid flow through numerical simulation and history matching. The obtained results illustrate the flexibility of the trained generator to produce sedimentary models that simultaneously match a given fluid flow behavior and complex geometries. The McMC method is

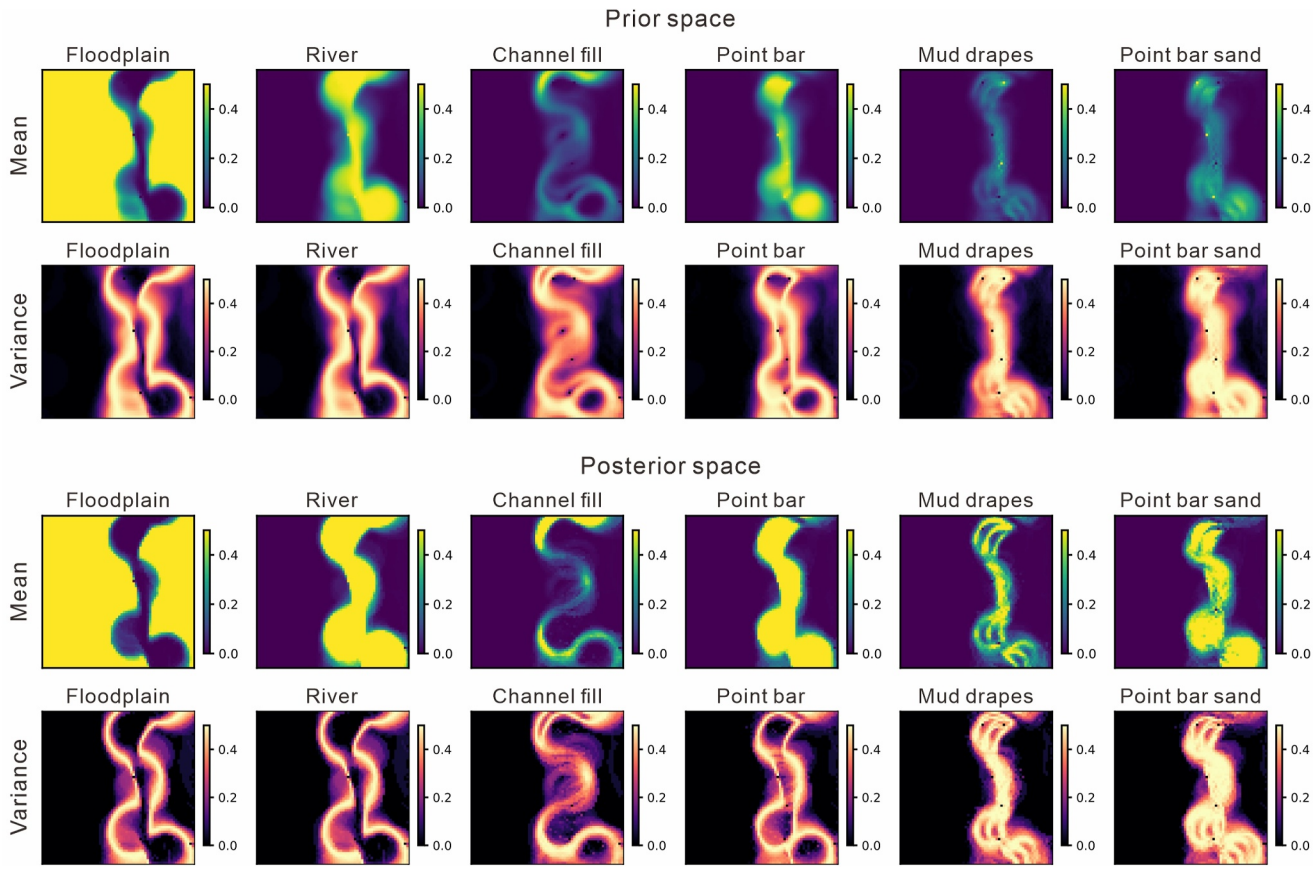

Figure 21. The mean and variance results for the prior and posterior spaces in the ground case. Columns 1–2: uncertainties of large-scale floodplain and river channels, identifiable under probability data. Columns 3–4: uncertainty of middle-scale channel fill and point bars. Columns 5–6: uncertainty of small-scale mud drapes and point bar sand, significantly reduced by dynamic numerical simulation. Both the mean and variance plots have the same color bar limits [0, 0.5].

used with the same manner as in Song et al. (2023) to perturb the simulated geomodel for history matching technique in this study; alternative optimization or sampling methods could also be used.

8. Conclusions

We propose herein the ALLUVSIM-GANSim workflow, which focuses on stochastic modeling of thin mud drapes inside the point bar reservoirs leveraging deep learning. The following conclusions were drawn.

1. Improved ALLUVSIM proves suitable for unconditional simulating a large number of reliable and diverse mud drapes models, making it a suitable training data set for GAN-based geomodeling methods. The characteristics of channel bars, including low and high channel sinuosity, as well as asymmetrical and symmetrical mud drapes, are accurately represented.
2. With the unconditional training data, the trained unconditional generator excels in capturing complex mud drapes patterns compared to unconditional MPS, making them a viable substitute to improve ALLUVSIM.
3. With the conditional training data set consisting of facies models, well-interpreted facies data, and probability maps, the trained conditional generator under the GANSim workflow exhibits powerful mud-drapes-feature extraction capabilities, and the ability to incorporate different types of information for producing multiple realizations.
4. The pre-trained conditional generator, derived from the synthesized mud drapes data, has demonstrated its capacity to expand to modern meandering river scenarios through high order statistics and dynamic history matching results. Furthermore, BHP inversion plays a significant role in reducing mud drapes uncertainty.

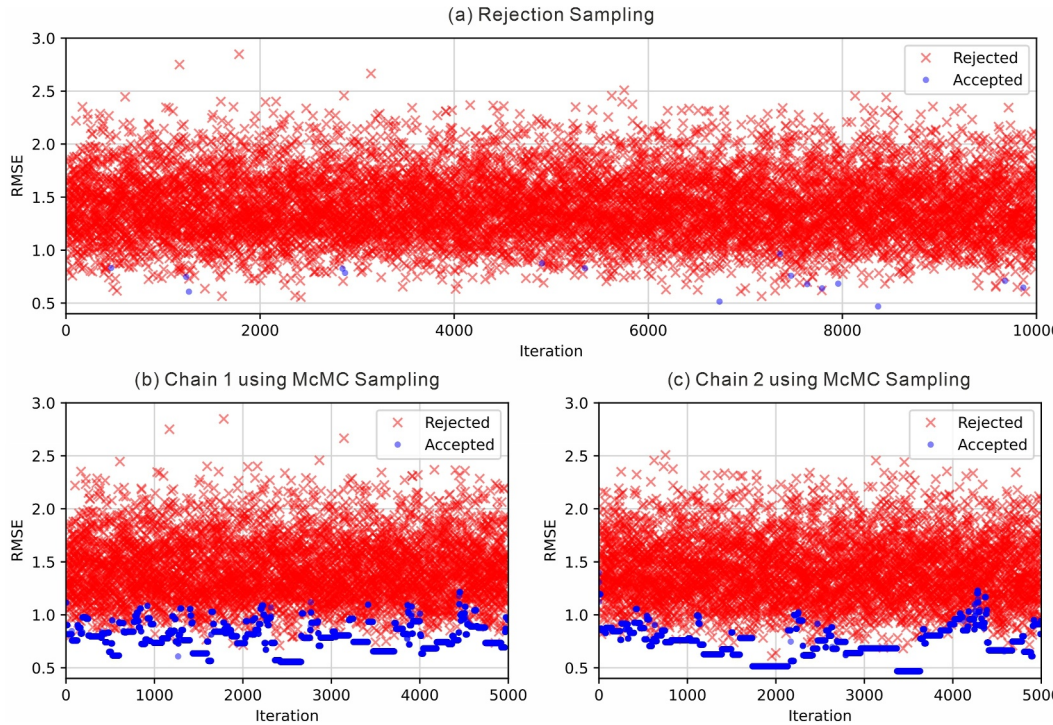

Figure 22. Bottomhole pressure inversion process: (a) adopts rejection sampling, while (b) and (c) adopt Markov chain Monte Carlo sampling. Red crosses and blue circles represent rejected and accepted models during the inversion, respectively.

Data Availability Statement

The data on which this study is based are available in Hu et al. (2024), including mud drapes data set, unconditional GAN code, and conditional GAN code.

Acknowledgments
This work was supported by the National Natural Science Foundation of China(No 42072146). LA gratefully acknowledges the support of the CERENA (FCT-UIDB/04028/2020). Hu, X., acknowledges financial support from the China Scholarship Council in a one-year visit to the University of Lisbon, which facilitated the writing and completion of this paper.

References

Al-Khalifa, M. A., Payenberg, T. H. D., & Lang, S. C. (2007). Overcoming the challenges of building 3D stochastic reservoir models using conceptual geological models—A case study. *Paper presented at the SPE Middle East Oil and Gas Show and Conference*, SPE-104496. https://doi.org/10.2118/104496-MS

Arjovsky, M., Chintala, S., & Bottou, L. (2017). *Wasserstein GAN. ArXiv preprint*. arXiv: 1701.07875.

Azevedo, L., Paneiro, G., Santos, A., & Soares, A. (2020). Generative adversarial network as a stochastic subsurface model reconstruction. *Computational Geosciences*, *24*(4), 1673–1692. https://doi.org/10.1007/s10596-020-09978-x

Biber, K., Khan, S., Janok, B., Barton, M., & Glennie, C. (2017). Quantitative characterization of shales within tidally influenced fluvial valley fill deposits of the Ferron Sandstone, eastern Utah: Implications for hydrocarbon exploration. *AAPG Bulletin*, *101*(10), 1599–1623. https://doi.org/10.1306/01111715108

Bridge, J. S., & Diemer, J. A. (1983). Quantitative interpretation of an evolving ancient river system. *Sedimentology*, *30*(5), 599–623. https://doi.org/10.1111/j.1365-3091.1983.tb00698.x

Chan, S., & Elsheikh, A. H. (2019). Parametric generation of conditional geological realizations using generative neural networks. *Computational Geosciences*, *23*(5), 925–952. https://doi.org/10.1007/s10596-019-09850-7

Colombera, L., Yan, N., McCormick-Cox, T., & Mountney, N. P. (2018). Seismic-driven geoce-llular modeling of fluvial meander-belt reservoirs using a rule-based method. *Marine and Petroleum Geology*, *93*, 553–569. https://doi.org/10.1016/j.marpetgeo.2018.03.042

Dawuda, I., & Srinivasan, S. (2022a). A hierarchical stochastic modeling approach for representing point bar geometries and petrophysical property variations. *Computers and Geosciences*, *164*, 105127. https://doi.org/10.1016/j.cageo.2022.105127

Dawuda, I., & Srinivasan, S. (2022b). Geologic modeling and ensemble-based history matching for evaluating CO2 sequestration potential in point bar reservoirs. *Frontiers in Energy Research*, *10*, 867083. https://doi.org/10.3389/fenrg.2022.867083

Deutsch, C. V., & Journel, A. G. (1998). *GSLIB: Geostatistical software library and user's guide*. Oxford University Press.

Deutsch, C. V., & Tran, T. T. (2002). FLUVSIM: A program for object-based stochastic modeling of fluvial depositional systems. *Computers and Geosciences*, *28*(4), 525–535. https://doi.org/10.1016/S0098-3004(01)00075-9

Dupont, E., Zhang, T., Tilke, P., Liang, L., & Bailey, W. J. (2018). *Generating realistic geology conditioned on physical measurements with generative adversarial networks*. ArXiv Preprint, arXiv: 1802.03065.

Ferguson, R. I. (1976). Disturbed periodic model for river meanders. *Earth Surface Processes*, *1*(4), 337–347. https://doi.org/10.1002/esp.3290010403

Gelman, A., Roberts, G. O., & Gilks, W. R. (1996). Efficient Metropolis jumping rules. In J. M. Bernardo, J. O. Berger, A. P. Dawid, & A. F. M. Smith (Eds.), *Bayesian statistics 5: Proceedings of the fifth valencia international meeting* (pp. 599–608). Oxford University Press.

Goodfellow, I. J., Pouget-Abadie, J., Mirza, M., Xu, B., Warde-Farley, D., Ozair, S., et al. (2014). Generative adversarial nets. In *International conference on neural information processing systems* (pp. 2672–2680). MIT Press.

Gulrajani, I., Ahmed, F., Arjovsky, M., Dumoulin, V., & Courville, A. (2017). Improved training of wasserstein GANs. In *Proceedings of the 31st international conference on neural information processing systems* (pp. 5769–5779). Curran Associates Inc. Retrieved from. https://doi.org/10.48550/arXiv.1710.10196

Hassanpour, M. M., Pyrcz, M. J., & Deutsch, C. V. (2013). Improved geostatistical models of inclined heterolithic strata for McMurray Formation, Alberta, Canada. *AAPG Bulletin*, *97*(7), 1209–1224. https://doi.org/10.1306/01021312054

Hastings, W. (1970). Monte Carlo sampling methods using Markov chains and their application. *Biometrika*, *57*(1), 97–109. https://doi.org/10.1093/biomet/57.1.97

Ho, J., Jain, A., & Abbeel, P. (2020). *Denoising diffusion probabilistic models*. ArXiv Preprint, arXiv: 2006.11239.

Hochreiter, S., & Schmidhuber, J. (1997). Long short-term memory. *Neural Computation*, *9*(8), 1735–1780. https://doi.org/10.1162/neco.1997.9.8.1735

Hoffimann, J., Fiorini, S. R., de Carvalho, B., Codas, A., Raoni, C., Zadrozny, B., et al. (2021). Probabilistic knowledge-based characterization of conceptual geological models. *Applied Computing and Geosciences*, *10*, 100055. https://doi.org/10.1016/j.acags.2021.100055

Howard, A. D. (1992). Modeling channel migration and floodplain sedimentation in meandering streams. In P. Carling & G. Petts (Eds.), *Lowland floodplain rivers: Geomorphological perspectives* (pp. 1–41). Wiley.

Howard, A. D., & Knutson, T. R. (1984). Sufficient conditions for river meandering: A simulation approach. *Water Resources Research*, *20*(11), 1659–1667. https://doi.org/10.1029/WR020i011p01659

Hu, X., Hou, J., Yin, Y., Liu, Y., Wang, L., Kang, Q., & Hou, M. (2023). A multi-scale blocking moving window algorithm for geostatistical seismic inversion. *Computers and Geosciences*, *173*, 105313. https://doi.org/10.1016/j.cageo.2023.105313

Hu, X., Song, S., Hou, J., Yin, Y., Hou, M., & Azevedo, L. (2024). Stochastic modelling of thin mud drapes inside point bar reservoirs with ALLUVSIM-GANSim (v1.0.0) [Dataset]. *Zenodo*. https://doi.org/10.5281/zenodo.10514223

Jeong, C., Mukerji, T., & Mariethoz, G. (2017). A fast approximation for seismic inverse modeling: Adaptive spatial resampling. *Mathematical Geosciences*, *49*(7), 845–869. https://doi.org/10.1007/s11004-017-9693-y

Johnson, S. M., & Dashtgard, S. E. (2014). Inclined heterolithic stratification in a mixed tidal–fluvial channel: Differentiating tidal versus fluvial controls on sedimentation. *Sedimentary Geology*, *301*, 41–53. https://doi.org/10.1016/j.sedgeo.2013.12.004

Karras, T., Aila, T., Laine, S., & Lehtinen, J. (2017). *Progressive growing of GANs for improved quality, stability, and variation*. ArXiv Preprint, arXiv: 1710.10196.

Kirillov, A., Mintun, E., Ravi, N., Mao, H., Rolland, C., Gustafson, L., et al. (2023). *Segment anything*. ArXiv Preprint, arXiv: 2304.02643.

Kolla, V., Posamentier, H. W., & Wood, L. J. (2007). Deep-water and fluvial sinuous channels—Characteristics, similarities and dissimilarities, and modes of formation. *Marine and Petroleum Geology*, *24*(6), 388–405. https://doi.org/10.1016/j.marpetgeo.2007.01.007

Labrecque, P. A., Jensen, J. L., Hubbard, S. M., & Nielsen, H. (2011). Sedimentology and stratigraphic architecture of a point bar deposit, Lower Cretaceous McMurray Formation, Alberta, Canada. *Bulletin of Canadian Petroleum Geology*, *59*(2), 147–171. https://doi.org/10.2113/gscpgbull.59.2.147

Laloy, E., Hérault, R., Jacques, D., & Linde, N. (2018). Training-image based geostatistical inversion using a spatial generative adversarial neural network. *Water Resources Research*, *54*(1), 381–406. https://doi.org/10.1002/2017WR022148

Laloy, E., Linde, N., Jacques, D., & Mariethoz, G. (2016). Merging parallel tempering with sequential geostatistical resampling for improved posterior exploration of high-dimensional subsurface categorical fields. *Advances in Water Resources*, *90*, 57–69. https://doi.org/10.1016/j.advwatres.2016.02.008

Lecun, Y., Bottou, L., Bengio, Y., & Haffner, P. (1998). Gradient-based learning applied to document recognition. *Proceedings of the IEEE*, *86*(11), 2278–2324. https://doi.org/10.1109/5.726791

Li, H., & Caers, J. (2011). Geological modelling and history matching of multi-scale flow barriers in channelized reservoirs: Methodology and application. *Petroleum Geoscience*, *17*(1), 17–34. https://doi.org/10.1144/1354-079309-825

Li, H., & White, C. D. (2003). Geostatistical models for shales in distributary channel point bars (Ferron sandstone, Utah): From ground-penetrating radar data to three-dimensional flow modeling. *AAPG Bulletin*, *87*(12), 1851–1868. https://doi.org/10.1306/07170302044

Lopez, S., Galli, A., & Cojan, I. (2001). Channelized reservoir modeling: A stochastic process-based approach. In *Paper presented at the international association of mathematical geologists*.

Makaske, B., & Weerts, H. J. T. (2005). Muddy lateral accretion and low stream power in a sub-recent confined channel belt, Rhine-Meuse delta, central Netherlands. *Sedimentology*, *52*(3), 651–668. https://doi.org/10.1111/j.1365-3091.2005.00713.x

Mariéthoz, G., & Caers, J. K. (2014). *Multiple-point geostatistics: Stochastic modeling with training images*. John Wiley and Sons. https://doi.org/10.1002/9781118662953

Mariethoz, G., Renard, P., & Straubhaar, J. (2010). The Direct Sampling method to perform multiple-point geostatistical simulations. *Water Resources Research*, *46*(11). https://doi.org/10.1029/2008WR007621

Mariethoz, G., Straubhaar, J., Renard, P., Chugunova, T., & Biver, P. (2015). Constraining distance-based multipoint simulations to proportions and trends. *Environmental Modelling and Software*, *72*, 184–197. https://doi.org/10.1016/j.envsoft.2015.07.007

Metropolis, N., Rosenbluth, A. W., Rosenbluth, M. N., Teller, A. H., & Teller, E. (1953). Equation of state calculations by fast computing machines. *The Journal of Chemical Physics*, *21*(6), 1087–1092. https://doi.org/10.1063/1.1699114

Montero, J., Colombera, L., Yan, N., & Mountney, N. (2021). A workflow for modelling fluvial meander-belt successions: Combining forward stratigraphic modelling and multi-point geostatistics. *Journal of Petroleum Science and Engineering*, *201*, 108411. https://doi.org/10.1016/j.petrol.2021.108411

Nesvold, E., & Mukerji, T. (2021). Simulation of fluvial patterns with GANs trained on a data set of satellite imagery. *Water Resources Research*, *57*(5), e2019WR025787. https://doi.org/10.1029/2019WR025787

Niu, B., Bao, Z., Yu, D., Zhang, C., Long, M., Su, J., et al. (2021). Hierarchical modeling method based on multilevel architecture surface restriction and its application in point-bar internal architecture of a complex meandering river. *Journal of Petroleum Science and Engineering*, *205*, 108808. https://doi.org/10.1016/j.petrol.2021.108808

Novakovic, D., White, C. D., Corbeanu, R. M., Hammon Iii, W. S., Bhattacharya, J. P., & McMechan, G. A. (2002). Hydraulic effects of shales in fluvial-deltaic deposits: Ground-penetrating radar, outcrop observations, geostatistics, and three-dimensional flow modeling for the Ferron sandstone, Utah. *Mathematical Geology*, *34*(7), 857–893. https://doi.org/10.1023/A:1020980711937

Park, T., Liu, M. Y., Wang, T. C., & Zhu, J. Y. (2019). Semantic image synthesis with spatially-adaptive normalization. In *Paper presented at the 2019 IEEE/CVF conference on computer vision and pattern recognition (CVPR)*. https://doi.org/10.1109/CVPR.2019.00244

Pranter, M. J., Ellison, A. I., Cole, R. D., & Patterson, P. E. (2007). Analysis and modeling of intermediate-scale reservoir heterogeneity based on a fluvial point-bar outcrop analog, Williams Fork Formation, Piceance Basin, Colorado. *AAPG Bulletin*, *91*(7), 1025–1051. https://doi.org/10.1306/02010706102

Pyrcz, M. J., Boisvert, J. B., & Deutsch, C. V. (2009). ALLUVSIM: A program for event-based stochastic modeling of fluvial depositional systems. *Computers and Geosciences*, *35*(8), 1671–1685. https://doi.org/10.1016/j.cageo.2008.09.012

Pyrcz, M. J., & Deutsch, C. V. (2004). Stochastic modeling of inclined heterolithic stratification with the bank retreat model. In *Paper presented at the proceedings of the 2004*. Canadian Society of Petroleum Geologists.

Rongier, G., Collon, P., & Renard, P. (2017). A geostatistical approach to the simulation of stacked channels. *Marine and Petroleum Geology*, *82*, 318–335. https://doi.org/10.1016/j.marpetgeo.2017.01.027

Russell, C. E., Mountney, N. P., Hodgson, D. M., & Colombera, L. (2018). A novel approach for prediction of lithological heterogeneity in fluvial point-bar deposits from analysis of meander morphology and scroll-bar pattern. *Fluvial meanders and their sedimentary products in the rock record*, 385–417. https://doi.org/10.1002/9781119424437.ch15

Shu, X., Hu, Y., Jin, B., Dong, R., Zhou, H., & Wang, J. (2015). Modeling method of point bar internal architecture of meandering river reservoir based on meander migration process inversion algorithm and virtual geo-surfaces automatic fitting technology. In *Paper presented at the SPE annual technical conference and exhibition*. https://doi.org/10.2118/175013-ms

Song, S., Mukerji, T., & Hou, J. (2021a). GANSim: Conditional facies simulation using an improved progressive growing of generative adversarial networks (GANs). *Mathematical Geosciences*, *53*(7), 1413–1444. https://doi.org/10.1007/s11004-021-09934-0

Song, S., Mukerji, T., & Hou, J. (2021b). Geological facies modeling based on progressive growing of generative adversarial networks (GANs). *Computational Geosciences*, *25*(3), 1251–1273. https://doi.org/10.1007/s10596-021-10059-w

Song, S., Mukerji, T., & Hou, J. (2022). Bridging the gap between geophysics and geology with generative adversarial networks. *IEEE Transactions on Geoscience and Remote Sensing*, *60*, 1–11. https://doi.org/10.1109/tgrs.2021.3066975

Song, S., Mukerji, T., Hou, J., Zhang, D., & Lyu, X. (2022). GANSim-3D for conditional geomodeling: Theory and field application. *Water Resources Research*, *58*(7), e2021WR031865. https://doi.org/10.1029/2021WR031865

Song, S., Zhang, D., Mukerji, T., & Wang, N. (2023). GANSim-surrogate: An integrated framework for stochastic conditional geomodelling. *Journal of Hydrology*, *620*, 129493. https://doi.org/10.1016/j.jhydrol.2023.129493

Straubhaar, J., Renard, P., & Chugunova, T. (2020). Multiple-point statistics using multi-resolution images. *Stochastic Environmental Research and Risk Assessment*, *34*(2), 251–273. https://doi.org/10.1007/s00477-020-01770-8

Strebelle, S. (2002). Conditional simulation of complex geological structures using multiple-point statistics. *Mathematical Geology*, *34*(1), 1–21. https://doi.org/10.1023/A:1014009426274

Sun, C., Demyanov, V., & Arnold, D. (2023). Geological realism in Fluvial facies modelling with GAN under variable depositional conditions. *Computational Geosciences*, *27*(2), 203–221. https://doi.org/10.1007/s10596-023-10190-w

Sun, T., Meakin, P., Jøssang, T., & Schwarz, K. (1996). A simulation model for meandering rivers. *Water Resources Research*, *32*(9), 2937–2954. https://doi.org/10.1029/96WR00998

Thomas, R., Smith, D., Wood, J., Visser, J., Calverley-Range, E., & Koster, E. (1987). Inclined heterolithic stratification—Terminology, description, interpretation and significance. *Sedimentary Geology*, *53*(1–2), 123–179. https://doi.org/10.1016/S0037-0738(87)80006-4

Wang, L., Yin, Y., Wang, H., Zhang, C., Feng, W., Liu, Z., et al. (2021). A method of reconstructing 3D model from 2D geological cross-section based on self-adaptive spatial sampling: A case study of cretaceous McMurray reservoirs in a block of Canada. *Petroleum Exploration and Development*, *48*(2), 407–420. https://doi.org/10.1016/S1876-3804(21)60032-0

Willis, B. J., & White, C. D. (2000). Quantitative outcrop data for flow simulation. *Journal of Sedimentary Research*, *70*(4), 788–802. https://doi.org/10.1306/2DC40938-0E47-11D7-8643000102C1865D

Winkels, T. G., Stouthamer, E., & Cohen, K. M. (2022). Planform architecture, meander evolution and grain-size variability of a deltaic channel belt in the Rhine-Meuse delta, The Netherlands. *Sedimentology*, *69*(7), 2844–2866. https://doi.org/10.1111/sed.13022

Yan, N., Colombera, L., & Mountney, N. P. (2021). Controls on fluvial meander-belt thickness and sand distribution: Insights from forward stratigraphic modelling. *Sedimentology*, *68*(5), 1831–1860. https://doi.org/10.1111/sed.12830

Yan, N., Mountney, N. P., Colombera, L., & Dorrell, R. M. (2017). A 3D forward stratigraphic model of fluvial meander-bend evolution for prediction of point-bar lithofacies architecture. *Computers and Geosciences*, *105*, 65–80. https://doi.org/10.1016/j.cageo.2017.04.012

Yin, Y. (2013). A new stochastic modeling of 3-D mud drapes inside point bar sands in meandering river deposits. *Natural Resources Research*, *22*(4), 311–320. https://doi.org/10.1007/s11053-013-9219-3

Yin, Y., Hu, X., Huang, J., Feng, W., Zhang, W., Taizhong, D., et al. (2020). A three-dimensional model of deep-water turbidity channel in plutonio oilfield, Angola: From training image generation, optimization to multi-point geostatistical modelling. *Journal of Petroleum Science and Engineering*, *195*, 107650. https://doi.org/10.1016/j.petrol.2020.107650

Zhang, T. F., Tilke, P., Dupont, E., Zhu, L. C., Liang, L., & Bailey, W. (2019). Generating geologically realistic 3D reservoir facies models using deep learning of sedimentary architecture with generative adversarial networks. *Petroleum Science*, *16*(3), 541–549. https://doi.org/10.1007/s12182-019-0328-4

References From the Supporting Information

Yin, Y., Chen, H., Huang, J., Feng, W., Liu, Y., & Gao, Y. (2020). Muddy interlayer forecasting and an equivalent upscaling method based on tortuous paths: A case study of mackay river oil sand reservoirs in Canada. *Petroleum Exploration and Development*, *47*(6), 1291–1298. https://doi.org/10.1016/S1876-3804(20)60136-2